Publications of the Astronomical Society of the Pacific, 131:084201 (35pp), 2019 August https://doi.org/10.1088/1538-3873/ab1d77

Variables in the Southern Polar Region Evryscope 2016 Data Set

Jeffrey K. Ratzloff[1], Henry T. Corbett[1], Nicholas M. Law[1], Brad N. Barlow[2], Amy Glazier[1], Ward S. Howard[1], Octavi Fors[1,3], Daniel del Ser[1,3], and Trifon Trifonov[4]

[1] Department of Physics and Astronomy, University of North Carolina at Chapel Hill, Chapel Hill, NC 27599-3255, USA; jeff215@live.unc.edu
[2] Department of Physics and Astronomy, High Point University, High Point, NC 27268, USA
[3] Institut de Ciències del Cosmos (ICCUB), Universitat de Barcelona, IEEC-UB, Martí i Franquès 1, E08028 Barcelona, Spain
[4] Max-Planck-Institut für Astronomie, Königstuhl 17, D-69117 Heidelberg, Germany
Received 2019 February 14; accepted 2019 April 28; published 2019 June 25

Abstract

The regions around the celestial poles offer the ability to find and characterize long-term variables from ground-based observatories. We used multi-year Evryscope data to search for high-amplitude (≈5% or greater) variable objects among 160,000 bright stars ($m_v < 14.5$) near the South Celestial Pole. We developed a machine-learning-based spectral classifier to identify eclipse and transit candidates with M-dwarf or K-dwarf host stars, and potential low-mass secondary stars or gas-giant planets. The large amplitude transit signals from low-mass companions of smaller dwarf host stars lessens the photometric precision and systematics removal requirements necessary for detection, and increases the discoveries from long-term observations with modest light-curve precision among the faintest stars in the survey. The Evryscope is a robotic telescope array that observes the Southern sky continuously at 2-minute cadence, searching for stellar variability, transients, transits around exotic stars and other observationally challenging astrophysical variables. The multi-year photometric stability is better than 1% for bright stars in uncrowded regions, with a 3σ limiting magnitude of $g = 16$ in dark time. In this study, covering all stars $9 < m_v < 14.5$, in declinations $-75°$ to $-90°$, and searching for high-amplitude variability, we recover 346 known variables and discover 303 new variables, including 168 eclipsing binaries. We characterize the discoveries and provide the amplitudes, periods, and variability type. A 1.7 R_J planet candidate with a late K-dwarf primary was found and the transit signal was verified with the PROMPT telescope network. Further follow-up revealed this object to be a likely grazing eclipsing binary system with nearly identical primary and secondary K5 stars. Radial-velocity measurements from the Goodman Spectrograph on the 4.1 meter SOAR telescope of the likely lowest-mass targets reveal that six of the eclipsing binary discoveries are low-mass (.06–.37 $M_\odot$) secondaries with K-dwarf primaries, strong candidates for precision mass–radius measurements.

Key words: (stars:) binaries: eclipsing – (stars:) Hertzsprung-Russell and C-M diagrams – stars: variables: general – planets and satellites: detection – planets and satellites: gaseous planets

Online material: color figures

1. Introduction

Variable star discoveries provide information on stellar properties, formation, and evolution, and are critical for determining distances and ages of astronomical objects. Eclipsing binaries allow the measurement of masses, radii, and temperatures, and can be used to test stellar formation theory predictions. Lower mass eclipsing binaries are observationally challenging due to the low intrinsic brightness of the star, and more systems are needed to properly characterize the mass/radius relationship in stellar models (Torres 2010; Mann et al. 2015; Kraus et al. 2017). Ground-based surveys such as the Palomar Transient Factory (Law et al. 2009), ATLAS (Tonry 2011), HAT (Bakos et al. 2004), HAT-South (Bakos 2018), SuperWASP (Pollacco et al. 2006), KELT (Pepper et al. 2007), CSTAR (Wang et al. 2015), and many others are very successful in detecting variables (including transiting exoplanets) and adding to known variable star catalogs such as the Variable Star Index[5] (VSX). These surveys either observe at day or longer timescale cadences, or observe dedicated sky areas to reach fast cadence at the expense of all-sky coverage. In contrast, the Evryscope is optimized for shorter-timescale observations with continuous all-sky coverage and a multi-year period observation strategy. The continuous, fast-cadence, all-sky Evryscope light curves are sensitive to variations (including transits and eclipses) lasting only a few minutes, and provide fine sampling for ten minute level variations or longer.

The Evryscope is a robotic camera array mounted into a 6 ft-diameter hemisphere which tracks the sky (Law et al. 2015).

[5] http://www.aavso.org/vsx/

The telescope is located at CTIO in Chile and observes continuously, covering 8150 sq. deg. in each 120 s exposure. The Evryscope was deployed with 22 cameras and can accommodate 27 total cameras (with a corresponding increased field of view of 10,000 sq. deg). Each camera features a 29MPix CCD providing a plate scale of 13″/pixel. The Evryscope monitors the entire accessible Southern sky at 2-minute cadence, and the Evryscope database includes tens of thousands of epochs on 16 million sources. In this paper, we limited the search field to the region around the South Celestial Pole, and chose the brighter stars in order to maximize the number of epochs per source and minimize systematics.

The Southern Polar sky area is less explored than other parts of the sky, primarily due to the difficulty in reaching it. This is evidenced by the comparatively low number of planet, eclipsing binary, and variable star discoveries in this region. For example, the sky area in the declination region of −75° to −90° comprises 3.4% of the southern sky's total area; however, the VSX catalog of known variables in the same region accounts for only 1.2% of the southern sky total. Surveys of the Southern Polar sky region typically either use a telescope located at a low latitude South American site or an instrument in the Antarctic. The former choice can be challenging depending on the airmass of the target region, while the second poses engineering difficulties due to the harsh environment (Law et al. 2013; Wang et al. 2015).

We use the Evryscope to explore the Southern Polar region (declinations −75° to −90°). While the airmass is non-optimal (∼1.7 average), the Evryscope monitors the Southern Polar region continuously every night for the entire night at 2-minute cadence, with the same camera for multiple years. This long-term, same-camera coverage at short cadence results in many continuous data points with consistent airmass, and minimizes systematics. Targets in this region average over 60,000 epochs per year. Our observing strategy results in several hundred thousand light curves with targets ranging in brightness from $9 < m_v < 15$. The light curves have the precision necessary to potentially detect eclipsing binaries, variable stars, transiting gas-giant planets around small-cool host stars, and short-transit-time planets around small compact stellar remnants including white dwarfs and hot subdwarfs. With additional filtering, the light curves are precise enough to potentially detect gas-giant planets around bright solar type stars; we will address this in future work. These Evryscope light curves also facilitate searches with wide period ranges (for the Polar Search we searched from 3–720 hours), longer periods, and wide amplitude ranges. Long-period discoveries are typically non-interacting stars and are challenging to detect due to the low number of transits.

The primary target of this paper's search is eclipsing binaries, particularly low-mass and long-period systems. The secondary target of this paper's search is gas-giant planets around M-dwarf or late K-dwarf primaries. This survey relies on detection power to narrow the candidates and uses observations from mid 2016 to early 2017. The more challenging transiting exoplanet detections will be conducted with additional systematics removal steps, additional candidate filtering to push to lower power detections, and will use the full three plus year data set (Ratzloff et al. 2019).

Eclipsing binaries are the best calibrators for determining relations between mass, radius, luminosity, and temperature. Relatively few low-mass (M-dwarf or late K-dwarf secondary) eclipsing binaries have been discovered (Kraus et al. 2011; Law et al. 2012; Chaturvedi et al. 2018), and many are too faint for easy radial velocity follow-up measurements. This has limited our ability to measure the mass/radius relation at low masses, where many low-mass systems suggest larger radii than stellar models predict (Torres 2010; Mann et al. 2015; Kraus et al. 2017). This is particularly important for the determination of transiting planet radii around low-mass single stars, where some of the most exciting nearby planets are likely to be discovered (Ricker et al. 2014; Christ et al. 2019; Stassun et al. 2018).

In this paper, we report the discovery of 303 new variables including seven eclipsing binaries with low-mass secondary stars. We perform spectroscopic follow-up on select eclipsing binaries to confirm the stellar type and secondary size. Radial velocity measurements reveal that seven of the eclipsing binary discoveries are low-mass (.06–.34 $M_\odot$) secondaries with K-dwarf primaries.

In Section 2 we describe the Evryscope photometric observations that led to the discoveries as well as our analysis of the light curves and detection algorithms for identifying variables. In Section 3 we describe the follow-up observations performed for the low-mass eclipsing binaries including PROMPT (Reichart et al. 2005) follow-up photometry, identification spectra and radial velocity follow-up using the Goodman (Clemens et al. 2004) spectrograph on the 4.1 meter SOAR telescope and the CHIRON (Tokovinin et al. 2013) echelle spectrometer on the CTIO/SMARTS 1.5 meter telescope. In Section 4 we present and characterize our discoveries. We also detail our analysis of the radial velocity follow-up work including the Monte Carlo simulation to fit the masses, radii, and other parameters. We conclude in Section 5.

2. Observations and Variability Search

2.1. Evryscope Photometry

All eclipsing binary and variable discoveries were detected in a transit search of the polar region (declinations −75° to −90°). The observations were taken from 2016 August 9 to 2017 April 4. The exposure time was 120 s through a Sloan-g filter and each source typically had 16,000 epochs. We briefly describe the calibration and reduction of images and the construction of light curves; further details will be presented in an upcoming Evryscope instrumentation paper. Raw images

are filtered with a quality check, calibrated with masterflats and masterdarks, and have large-scale backgrounds removed using the custom Evryscope pipeline. Forced photometry is performed using APASS-DR9 (Henden et al. 2015) as our master reference catalog. Aperture photometry is performed on all sources using multiple aperture sizes; the final aperture for each source is chosen to minimize light-curve scatter. The primary systematics challenges are: background and airmass changes and the subsequent effects on stars of different magnitude and color, the ratchet observing cycle causing the targets to switch cameras and appear in different positions on the CCD chips over the observing season, daily aliases, source blending, PSF distortions, and vignetting. We use the quality filter, calibrations, aperture photometry, along with a custom implementation of the SysRem (Tamuz et al. 2005) algorithm to remove the systematics challenges described above.

2.2. Detection of Variables

Filtering by declination and magnitude returns 239,991 initial targets from the Evryscope light-curve database. 76,407 are eliminated by an additional quality filter based on non-blended sources. The remaining 163,584 are analyzed using Box Least Squares (BLS) (Kovacs et al. 2002; Ofir 2014) with the pre-filtering, daily-alias masking, and settings described in Section 2.4. The light curves are then sorted by BLS detection power, in terms of Signal Detection Efficiency (SDE) (Kovacs et al. 2002). Figure 1 shows the BLS SDE distribution for the targets along with the distribution of detected periods. Targets with an SDE > 10 and with nearby reference stars gives 9104 suspects for further inspection. The 10-SED cutoff is chosen to: (1) limit the number of targets to an amount that is reasonable for human follow-up (in this case $\sim$10,000); (2) ensure a reasonable chance of detecting high-amplitude candidates without accumulating excessive false positives; and (3) reach three percent level signal depths on bright stars to potentially detect low-mass secondaries and gas-giant planets around M-dwarfs or late K-dwarfs.

We compare the target light curve (both unfolded and folded to the best BLS period) with two nearby reference stars of similar magnitude looking for any signs that the detected variation is present in the references indicating systematics (see Section 2.5). The folded plots are colored by time to check how well mixed the detection is, as a transit or eclipse with only a single or few occurrences is more likely to be an artifact of the detection algorithm. The light curves are also folded on the second and third best BLS periods to check for aliases, as well as the best Lomb-Scargle (LS) (Lomb 1975; Scargle 1982) period to check for sinusoidal variability. From visual inspection, we identify 649 variables from the machine filtered 9104 suspects. 346 are known variables and 303 are new discoveries.

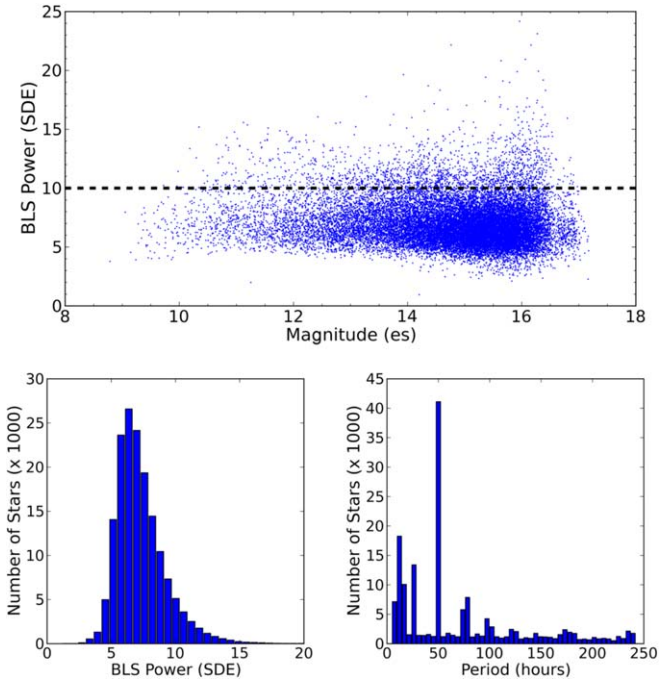

Figure 1. Detection characteristics from the BLS results of the polar search. The top panel shows the BLS power in SDE vs. magnitude (15% of the points are shown for better visualization); the lower left panel is the histogram of BLS power in SDE; the lower right is the histogram of periods found. Targets with an SDE > 10 are selected for further inspection.
(A color version of this figure is available in the online journal.)

2.3. Machine-learning Stellar Classification

We developed a machine-learning based classifier that uses publicly available catalog data to estimate stellar size from a B-V color/magnitude space, and to estimate spectral type from multiple color differences. The discovery candidates were matched to APASS-DR9 (Henden et al. 2015) and PPMXL (Roeser et al. 2010) catalogs to obtain reduced proper motion (RPM) and color differences (B-V, V-K, J-H, H-K) for each target. Modifying the method in Jones (1972) with a two step machine-learning process described below, we classify stars based on B-V and RPM to identify stellar size—main sequence, giants, white dwarfs, or subdwarfs. The RPM and B-V combination provides a high return on our target catalog (99% of our targets are classified as demonstrated below) and captures spectral information using available data. After the stellar size estimation is completed, the four color differences are used to approximate the spectral type.

In the first step of the machine-learning process, we use a support vector machine (SVM) from the SKYLEARN python module (Pedregosa et al. 2011) to identify likely hot subdwarfs (HSD) from all other stars. The HSD are challenging to separate since they can be close to main sequence O/A stars in this parameter space. We find the SVM to be an effective way

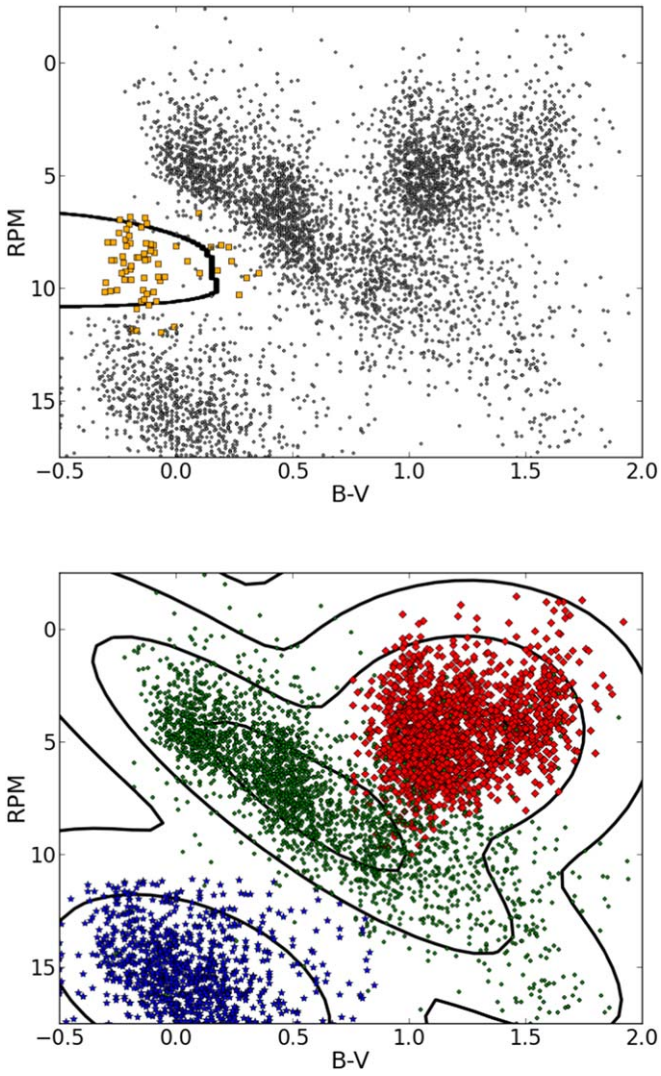

Figure 2. Evryscope Target Classification. We use B-V color differences and reduced proper motion (RPM) data with a two step machine-learning algorithm to classify star size. Top: the training data (gold squares = hot subdwarfs, grey = all others) for the support vector machine (SVM) which returns the resulting hot subdwarf classification region (the area inside the black border). Bottom: the training data (blue stars = white dwarfs, green = main sequence, red diamonds = giants) for the Gaussian Mixture Model (GMM) which returns the resulting classification contours. Negative-log likelihood plot-lines 1, 1.7, 2.8 are shown.
(A color version of this figure is available in the online journal.)

to segregate the HSD, shown in the top panel of Figure 2 as the small confined area enclosed in the black border. This is done by using a training set of HSD from (Geier et al. 2017) and other types of stars from SIMBAD (Wenger et al. 2000), filtering the outliers, then computing the contour boundaries. The SVM method is a non-probabilistic, two-class classifier that computes a hard boundary (decision boundary) by minimizing the distance (or margin) between the points closest to the boundary. As with any classifier there are missed targets and contaminants, and there are physical reasons the results can be skewed (reddening, for example). Our goal in this step is to separate the most challenging class (the HSD) from all the other classes while providing a boundary with a reasonable contingency space to the nearby white dwarf and main sequence regions.

Once the HSD are identified, all remaining objects are classified using a Gaussian Mixture Model (GMM; Pedregosa et al. 2011) with three classes to identify white dwarfs, main sequence, and giants. We again use an outlier filtered training set of stars of each type from SIMBAD (20,972 main sequence, 1515 white dwarfs (WD), and 10,000 giants). The GMM classifier results are shown in the bottom panel of Figure 2. The GMM method is a best fit to 2D Gaussian function (probability density function), using the training points to adjust the Gaussian centers, orientations, and elongations. Our application of this method uses three dimensions (WD, main sequence, and giants). Although more dimensions are possible, overlapping or poorly separated classes tend to give poor results (part of the motivation of using the SVM for the HSD step). The GMM produces contour lines with Negative-log-likelihood (NLL) values that can be converted ($LH = 10^{-NLL}$) to give an estimate of the confidence level the data point belongs in the class.

We use the spectral type and temperature profiles in (Pecaut & Mamajek 2013) to derive a function (using 1D interpolation) that uses available color differences to derive an estimate for spectral type (Figure 3). If only B-V is available, we classify simply by the letter (O, B, A, F, G, K, M); if multiple colors are available we average the fits and choose the closest spectral type (G9, K4, M3, for example). For main sequence stars we add the luminosity class V. The code produces a function with RPM and color differences inputs and outputs the star size, star type, and NLL score for the GMM step. We used this to classify all of our discoveries, with the added requirement that the HSD also be apparent spectral type O or B and that the WD have a NLL score of less than 4.0. The added requirements help filter contaminants from main sequence A stars for the HSD, and borderline WD stars. Candidates identified as likely K or M-dwarfs with shallow (typically less than 10%) eclipses or transits are identified as potentially high value targets and analyzed in more detail.

The Evryscope classifier is designed to (1) facilitate identification of as many of the target light curves as practical; (2) identify targets to be included in Evryscope transit searches (white dwarfs, hot subdwarfs, K- and M-dwarfs); and (3) classify variability discoveries helping to identify those as potentially interesting for further follow-up. For the Polar Search, 98.5% of our targets have B-V and RPM data available, and 91.0% have all four color differences and RPM data. Tests

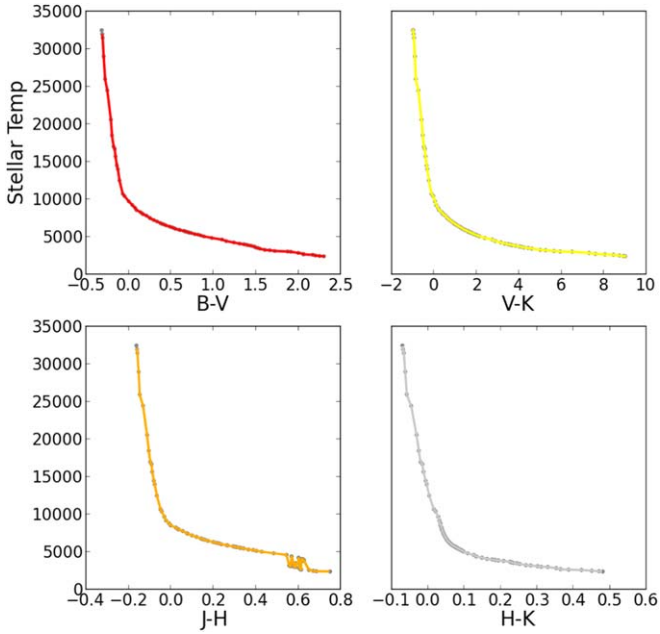

Figure 3. Evryscope Target Classification. We use (B-V, V-K, J-H, H-K) color differences to estimate temperature and spectral type using the data in (Pecaut & Mamajek 2013) to interpolate profiles for each color difference. The data are the grey points and the interpolations are the colored lines in the figures. We average the four results and pick the closest spectral type.
(A color version of this figure is available in the online journal.)

using 485,000 targets spread across the entire southern sky (all R.A. and declinations $+10^{\circ}$ to -90°) have demonstrated very high returns: 99% of Evryscope targets have all four color differences and RPM data available for classification. Once the catalogs were compiled and matched, the classifier took only a few minutes to classify the 485,000 test targets, making it practical for use on the full Evryscope database. All discoveries in this work are classified using the APASS-DR9 (Henden et al. 2015) and PPMXL (Roeser et al. 2010) catalogs as described above. A similar approach using the GAIA-DR2 (Gaia Collaboration et al. 2018) catalog will be used as an additional target filter for the transiting exoplanet searches (Ratzloff et al. 2019).

We tested the Evryscope classifier in several ways. We chose known WD from APASS (Raddi et al. 2017) and high confidence (>.80) WD suspects from ATLAS (Pietro Gentile Fusillo et al. 2017) and SDSS (Pietro Gentile Fusillo et al. 2015) with $m_v < 16.5$, for a total of 211 classifier test targets. Using Geier et al. (2017) with $m_v < 15.0$, we obtain 1560 HSD classifier test subjects (which may include WD due to the difficulty in separating the two groups). We use Lépine & Gaidos (2011) to obtain 3764 high-confidence M-dwarfs. Using Kharchenko (2001) and filtering out the bright stars we have 999 main sequence, 452 giants, and 895 K-dwarfs for classifier testing.

Table 1
Evryscope Classifier Star Size (ms/giant/WD/HSD) Performance

Test Group	Star Size	ES Classifier Percent Correct
M-dwarfs	ms	95.3%
K-dwarfs	ms	86.2%
M-giants	giant	98.7%
Main sequence	ms	94.1%
HSD	HSD	54.5 (77.7 w/WD)%
WD	WD	87.0%

Table 2
Evryscope Classifier Letter Spectral Type (O, B, A, F, G, K, M) Performance

Test Group	Letter Spectral Type	ES Classifier Percent Correct
M-dwarfs	M	95.2%
K-dwarfs	K	81.1%
M-giants	M	97.9%
Main Sequence	O-M	69.5%
HSD	O,B	76.5%

Table 3
Evryscope Classifier Full Spectral Type (O0—M9) Performance

Test Group	Spectral Type	Mean	ES Classifier Variance	% +/−3
M-dwarfs	M0-M9	−.50	1.9	95.3%
K-dwarfs	K0-K9	−.98	2.7	81.6%
M-giants	M0-M9	−2.0	1.7	78.0%
Main Sequence	O0–M9	−.87	3.7	63.1%

Note.
[a] Shown is the mean difference and variance in classifier performance numerical class versus the known class. The last column shows the percent of the test group that is classified correctly to within 3 of the known numerical class.

Table 1 shows the performance of the classifier to correctly determine star size (ms/giant/WD/HSD). Table 2 shows the performance of the classifier to correctly determine letter spectral type (O, B, A, F, G, K, M). Table 3 shows the performance of the classifier to correctly determine full spectral type (O0—M9).

We also compared the classifier results to SOAR ID spectra taken for the low-mass eclipsing binaries (Section 4.7). 7 of the 8 were classified as the correct spectral type (K for example), and within $+/-1$ numeric class (K5 or K6 for example) (Table 4).

2.4. Variability Search Algorithms

We selected sources in the polar region with $m_v < 14.5$ and with light curves that passed quality tests to eliminate sources with blending, narrow time coverage, or low number of epochs

Table 4
Comparison of the Evryscope Classifier with SOAR ID Spectra

ID (EVR+)	SOAR ID Sptp	ES Classifier Sptp
J053513.22-774248.2	G7V	K1V
J06456.10-823501.0	G8V	G9V
J103938.18-872853.8	K7V	K6V
J110815.96-870153.8	K4V	K3V
J165050.23-843634.6	K5V	K4V
J180826.26-842418.0	G5V	G6V
J184114.02-843436.8	K2V	K3V
J211905.47-865829.3	K5V	K6V

(Section 2.2). Light curves (with MJD timestamps) were pre-filtered with a Gaussian smoother to remove variations on periods greater than 30 days, and a third-order polynomial fit was subtracted to remove long-term variations. Light curves were then searched for transit-like, eclipse-like, and stellar variability signals using the Box Least Squares (BLS) (Kovacs et al. 2002; Ofir 2014) and Lomb-Scargle (LS) (Lomb 1975; Scargle 1982) algorithms.

We tested the recovery rates on Evryscope light curves with different BLS settings, with periods ranging from 2–720 hours, 10,000–100,000 periods tested, and transit fractions from .001 to 0.5. Recovery rate tests were run on known eclipsing binaries in our magnitude range with different transit depths ranging from .01 to .25, and on simulated few-percent level transit signals injected onto Evryscope light curves representative of low-mass secondaries. The tests showed that a very wide BLS test period range (2–720 hours) led to decreased detections as the periodogram becomes biased to long periods or spikes in longer periods arise from data gaps. This challenge combined with the survey 6-month time coverage (Section 1), shows too aggressive of a period range can detect fewer eclipsing binary candidates. Based on these tests, the final BLS settings used on the Evryscope Polar Search were a period range 3–250 hours with 25,000 periods tested and a transit fraction of .01 to .25.

Period detections of 24-hours and corresponding aliases (4, 6, 8, 16, 36, 48, and 72 hours) were masked in $+/-$ .1 hour widths. The results were sorted by BLS signal detection strength—BLS periodogram peak power in terms of sigmas above the mean power. Targets with peak power greater than 10σ were verified visually with a panel detection plot. We use the Lomb-Scargle (LS) algorithm to identify sinusoidal variables. For LS, we used a period range 3–720 hours to include sensitivity to longer period variables. We recover slightly lower amplitude variables (minimum discovery amplitude in this work =.008) than eclipsing binaries (minimum discovery depth in this work =.029) as shown in the Appendix.

Figure 4 shows the phase-folded Evryscope light curve for EVRJ110815.96-870153.8 a K4V primary and .21 $M_{\odot}$ secondary with a BLS detected period of 12.28 hours. Figure 5 shows the light curve for EVRJ032442.50-780853.9 a variable star with a LS detected period of 4.67 hours.

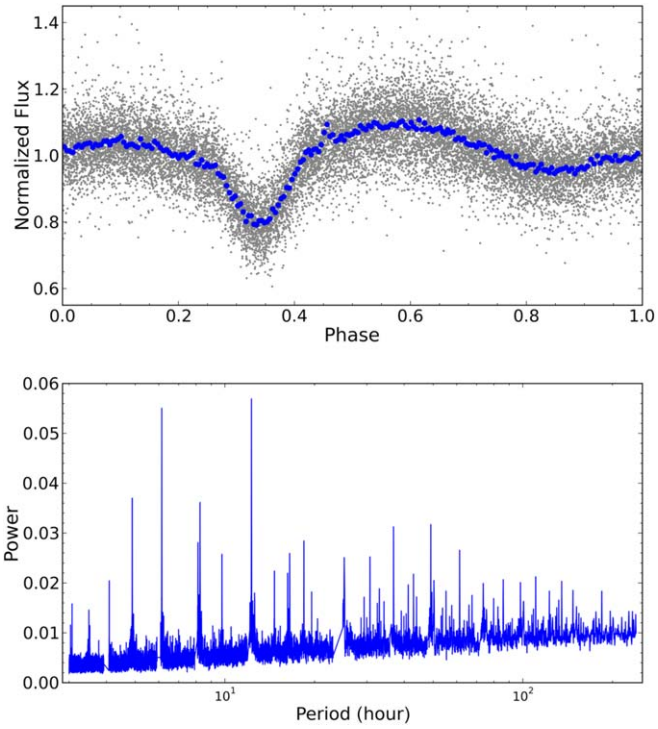

Figure 4. Example low-mass eclipsing binary discovery (EVRJ110815.96-870153.8) from this survey. The Evryscope light-curve phased on its period of 12.277 hours is shown on the top panel. Gray points = 2-minute cadence, blue points = binned in phase. The bottom panel shows the BLS power spectrum with the highest peak at the 12.277 hour detection.
(A color version of this figure is available in the online journal.)

2.5. False Positive Tests

We performed several tests to verify the variability signals were not false positives. First, we compared the candidate light curve with several nearby reference star light curves looking for similar variation to test for systematics or PSF blending. The nearest reference stars within 0.2 degrees of the reference star were filtered by magnitude and light-curve coverage. The nearest three with magnitudes within 0.5 mag of the target star and with a light-curve coverage and number of data points within 20% of the target light curve are chosen for comparison. The references are folded at the same period as the detected period of the candidate, and are inspected visually for signs of similar signals, offsets, or outliers. Candidates with references showing similar variability are assumed to be systematics and thrown out.

Next, we tested how well mixed in phase the observations were, with poor mixing potentially indicating matched-filter fits

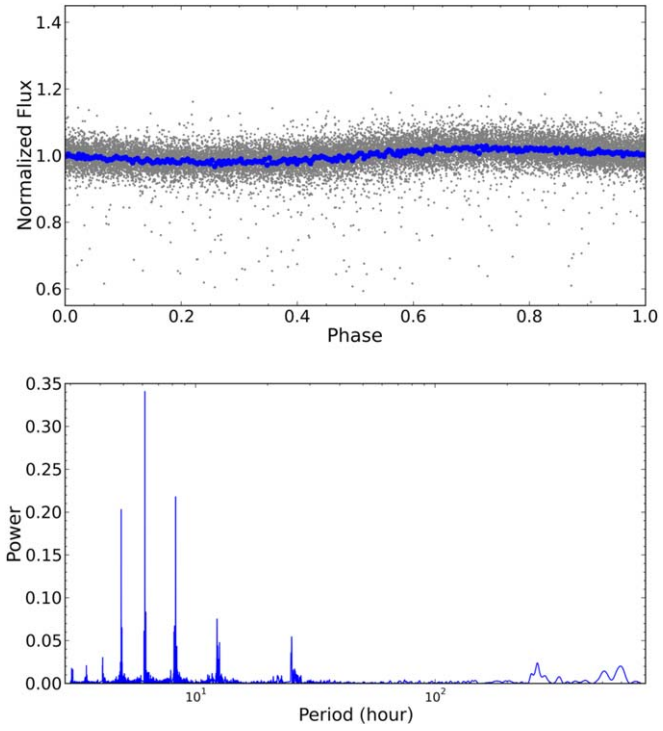

Figure 5. Example variable discovery (EVRJ032442.50-780853.9) from this survey. The Evryscope light-curve phased on its period of 4.676 hours is shown on the top panel. Gray points = 2-minute cadence, blue points = binned in phase. The bottom panel shows the LS power spectrum with the highest peak at the 4.676 hour detection.
(A color version of this figure is available in the online journal.)

to systematics or data gaps instead of astrophysical signals. This is performed by folding the candidate on the detected period and color coding the points by time (ranging from a blue-to-red scheme mapped to early-to-late times) and visually inspecting the resulting plot. For each discovery, we also compared the phased light curve of the first and the second half of the data looking for inconsistency. Candidates with marginal results from these tests were reviewed by an additional person and thrown out if both agreed the target is suspect.

Eclipsing binary light curves that did not reveal a secondary eclipse or out-of-transit ellipsoidal variation were tested further. For these candidates, we folded the light curves at twice the detected period, looking for differences in odd/even transit depths to rule out finding half of the actual period. Candidates passing these tests were then flagged as probable variable discoveries and analyzed further as detailed in Section 4.

3. Follow-up Observations

Follow-up observations for select eclipsing targets were made with the PROMPT telescopes (Reichart et al. 2005) to confirm the Evryscope detection. We used the SOAR Goodman spectrograph (Clemens et al. 2004) for stellar classification and intermediate-resolution radial velocity measurements. We used the CHIRON (Tokovinin et al. 2013) spectrograph for high-resolution radial velocity measurements to measure the companion masses of select suspected low-mass secondaries.

3.1. SOAR Goodman ID Spectroscopy

We observed the low-mass candidates on 2018 April 29 on the SOAR 4.1 m telescope at Cerro Pachon, Chile with the Goodman spectrograph. We used the red camera with the 400 1/mm grating with a GG-455 filter in M1 and M2 preset mode with 2x2 binning and the 1″ slit (R $\sim$ 825). The red camera[6] is optimized for the optical red part of the spectrum and when used with the M1 and M2 presets provides a wavelength coverage of 3500–9000 Å. The Goodman spectra are 2D, single order. We took eight consecutive 60 s spectra for each of the targets and for the standard LTT3864. For calibrations, we took 3 $\times$ 60 s FeAr lamps, 10 internal quartz flats using 50% quartz power and 10 s integrations, and 10 bias spectra.

We processed the spectra with a custom pipeline written in Python by the Evryscope team; this pipeline is described in detail here. The eight spectra for each target are median-combined, bias-subtracted, and flat-corrected. A third-order polynomial is fit to the brightest pixels in each row; the spectra are then extracted in a 10-pixel range and background subtracted. We identify 8 prominent lamp emission lines for each preset (including 3749, 4806, 6965 Å and many others spread across the entire wavelength range) and compare with the known lines of the Iron-Argon arc lamp using a Gaussian fit of each feature. We use a 4th-order polynomial to fit the Gaussian peaks and wavelength-calibrate each spectrum. We used the standard star LTT3864 to flux-calibrate by first removing prominent absorption features then fitting a seventh-order polynomial to the continuum. The resulting SOAR standard star spectra was visually matched to the template from the ESO library and verified to fit within the template precision. The spectra were normalized and the results from the M1 and M2 presets were combined for each target with a wavelength coverage of 3500–9000 Å.

Errors in the SOAR spectra arise from instrumentation systematics, observational conditions, and the extraction pipeline. Instrumentation error sources are dominated by flexure, component alignment, and limitations in optical quality due to manufacturing constraints; see Clemens et al. (2004) for an elaborate discussion of these contributions. Observational sources of errors are primarily due to background noise, airmass, and atmospheric effects. Errors in the spectra from the extraction process are discussed in detail in Fuchs et al. (2017); the chosen standard, normalization process, and resolution are the error sources relevant to this work. The Goodman spectrograph has been operating consistently for over 15 years,

[6] http://www.ctio.noao.edu/soar/content/goodman-red-camera

Table 5
PROMPT Observations of Select Targets

ID (EVR+)	Date	Images	B/R(s)
J06456.10-823501.0	Dec 10, 2017	412	40/20
J114225.51-793121.0	Oct 30, 2017	190	90/60
J114225.51-793121.0	Feb 16, 2018	288	90/60
J184114.02-843436.8	Dec 19, 2017	202	100/45
J211905.47-865829.3	Nov 21, 2017	120	130/90

and we use the accumulated knowledge to minimize errors from instrumentation, observation, and processing sources. In Section 4.2 we compare the SOAR ID spectra to the spectra of stars with known stellar types. The known spectra are from different instruments, observational strategies, and pipelines; additionally, the available known spectra are limited to an accuracy of ≈1–2 in the luminosity class. The combined errors in the high S/N SOAR ID spectra are less than this limitation. We demonstrate this in Section 4.2 by comparing the results from different stellar classification methods, which are consistent to ≈1–2 in the luminosity class.

3.2. PROMPT Photometry

EVRJ114225.51-793121.0, EVRJ06456.10-823501.0, EVR J184114.02-843436.8, and EVRJ211905.47-865829.3 were observed with the PROMPT P8 60 cm telescope located at CTIO Chile. All observations were taken with Johnson B and Johnson R filters, interleaved. Table 5 summarizes the PROMPT follow-up work.

The PROMPT follow-up observations confirm the candidate variability is astrophysical and not an Evryscope systematic by observing the Evryscope detection signal with a separate instrument and different eclipse time. The PROMPT telescopes have a 100 times larger aperture than the Evryscope cameras, giving the PROMPT light curves a lower root-mean-square (rms) scatter and improved signal-to-noise-ratio (S/N) compared with the Evryscope discovery light curves. The amount of improvement depends on many factors including target brightness and sky background; here we show a representative example, EVRJ211905.47-865829.3 in Figure 6. The light-curve rms (after removing the eclipse) for this target is .006 in PROMPT and .108 in Evryscope (unbinned 2-minute cadence). This corresponds to a S/N of ≈167 for the PROMPT single transit light curve and ≈9.5 for the Evryscope one year light curve. These results compare nicely to estimated theoretical S/N of 175 and 12 for PROMPT and Evryscope, respectively, using reasonable values for sky background, throughput, and airmass for these telescopes observing an $m_v = 14.0$ magnitude target. We point out that the Evryscope binned light curve can reach the S/N of the PROMPT light curve, in this example with reduced sampling. In our white dwarf/hot subdwarf fast binary discovery paper (Ratzloff et al. 2019), we demonstrate

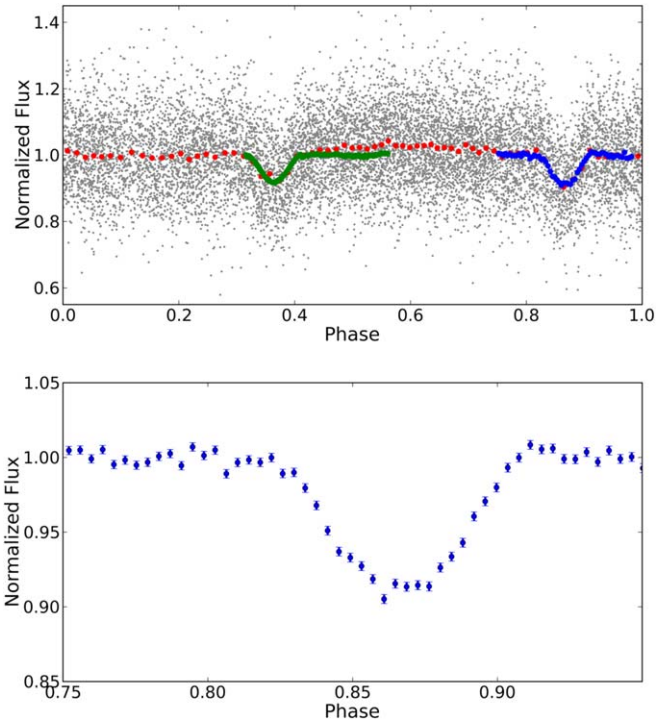

Figure 6. Top: combined light curves of EVRJ211905.47-865829.3. This object was flagged as a potential 9.3 hour transiting gas-giant planet as the transit depths are unchanged by color and in odd/even phase. There is a slight out of phase ellipsoidal variation when folded at the 18.6 hour period indicating it is most likely a grazing eclipsing binary with nearly identical primary and secondaries. Bottom: a detailed view of the transit in the PROMPT light curve with 1σ errors shown.
(A color version of this figure is available in the online journal.)

the ability to reach higher than PROMPT S/N with multiple year binned Evryscope data. In this work, we use PROMPT to verify the Evryscope candidates and better characterize the eclipse depth and shape to reduce the error in the companion radii calculation. For this target, we also observed the secondary eclipse for comparison with the primary eclipse shown in Figure 6. The PROMPT data also provides an additional eclipse time (several months past the latest Evryscope eclipse), and by phase-folding both light curves, the period accuracy is increased.

The PROMPT images were processed with a custom aperture photometry pipeline written in Python. The images were dark and bias-subtracted and flat-field-corrected using the master calibration frames. Five reference stars of similar magnitude are selected and aperture photometry is performed using a range of aperture sizes. The background is estimated using a sigma clipped annulus for each star scaled by the aperture size. A centroid step Gaussian fits the PSF to calculate the best center and ensures each aperture center is consistent regardless of pixel drift. The light-curve rms variation is computed for the range of apertures, and the lowest-variation aperture size is chosen. A

final detrending step using a third-order polynomial is applied to remove remaining systematics. Photometric errors are calculated per epoch using the estimated CCD aperture photometry noise in Merline & Howell (1995) and the atmospheric scintillation noise approach in Young (1967). A detailed summary of the photometric error calculation is given in Collins et al. (2017). We combined the PROMPT and Evryscope light curves for final inspection. An example of a grazing eclipsing binary originally flagged as a 1.7 R_J planet candidate is shown in Figure 6. Radial velocity follow-up with the HARPS (Mayor et al. 2003) spectrograph on the ESO La Silla 3.6 m telescope combined with the detailed light-curve analysis confirms the candidate is a grazing eclipsing binary.

3.3. Intermediate-resolution Spectroscopy and Radial Velocity

EVRJ114225.51-793121.0, EVRJ06456.10-823501.0, EVR J053513.22-774248.2, EVRJ184114.02-843436.8, and EVR J211905.47-865829.3 were observed on 2017 November 15 and 19 and December 15 and 16 on the SOAR 4.1 m telescope at Cerro Pachon, Chile, with the Goodman spectrograph. EVRJ110815.96-870153.8, EVRJ180826.26-842418.0, EVR J165050.23-843634.6, and EVRJ103938.18-872853.8 were observed on 2018 February 12 and March 3. We used the blue camera with the 2100 1/mm grating in custom mode with 1×2 binning and the $1''$ slit ($R \sim 5500$). We took four 300–360 s spectra depending on the target and conditions. For all targets, we took 3×60 s FeAr lamps after each group of science images. We took 10 internal quartz flats with 80% quartz lamp power and 60 s integration, and 10 bias spectra.

The spectra are processed using a modified version of the Python code described in Section 3.1 and radial velocity measurements are calculated (Section 4.3). The SOAR spectra return radial velocity precision of ≈10 km/s for our targets, which allows us to characterize the secondary mass for small late M-dwarf stars. This also allowed us to rule out potential planetary-mass secondaries—the case in several of the grazing eclipses.

3.4. High-resolution Radial Velocity

EVRJ06456.10-823501.0 and EVRJ053513.22-774248.2 were observed between 2018 January 28 and 2018 March 25 on seven nights (one data point per night) with the SMARTS 1.5 m telescope at CTIO, Chile with the CHIRON spectrograph. EVRJ184114.02-843436.8 was observed on 2018 March 23. Spectra were taken in image slicer mode ($R \sim 80000$). One 1500 to 1800 second spectrum was taken depending on the target and conditions. Spectra of RV standard HD131977 were taken to verify processing results.

Spectra were wavelength calibrated by the CHIRON pipeline, which we processed using a custom python code to measure radial velocity. We visually inspected the spectral orders and chose the top seven by S/N and with prominent atmospheric absorption features. The orders are spread throughout the wavelength range, and we select the most prominent atmospheric feature per order. Within each of the selected orders, for each observation, we clip a small section (typically 20 Å) encompassing the best absorption feature. For example order nine uses the 4957 Å feature, order 14 uses the 5328 Å feature, and order thirty-seven uses the 6563 Å feature. We fit a Lorentzian to the absorption features and measure the wavelength shift of each observation in each order. For each observation, we sigma clip any outlier orders and use the average shift to calculate the velocity. Using the standard deviation of the measured shifts between the orders, we place error limits. The error in the RV standard is measured to ≈200 m/s, while the errors in the fainter targets are ≈1 km/s. An example is shown in Figure 7; the best-fit RV amplitude from the CHIRON data is 69.0 km/s and for the SOAR data is 64.7 km/s.

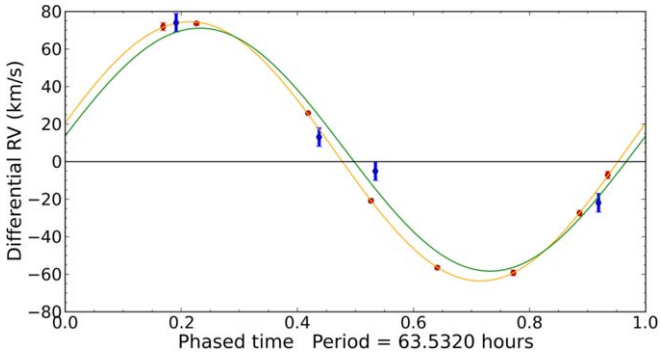

Figure 7. Combined Radial Velocity curves for target EVRJ06456.10-823501.0. The red data points are from CHIRON RV data, and the blue points are SOAR data with the yellow and green curves of best fit.
(A color version of this figure is available in the online journal.)

4. Discoveries

In this section we present the discoveries beginning with the eclipsing binaries and variables. We measure the amplitudes of the variation, and for select targets we use the radial velocity measurement to estimate the companion mass. We show distributions of the periods, amplitudes, and magnitudes of the discoveries and summarize the important statistics of the search. All results are summarized in the appendices; see Tables 8–11 and Figures 15–17.

4.1. Discovery Candidates Parameter Estimations

Candidates passing the false positive checks (Section 2.5) are separated by variation type (eclipse-like or sinusoidal variable-like) and measured. The eclipsing binary light curves

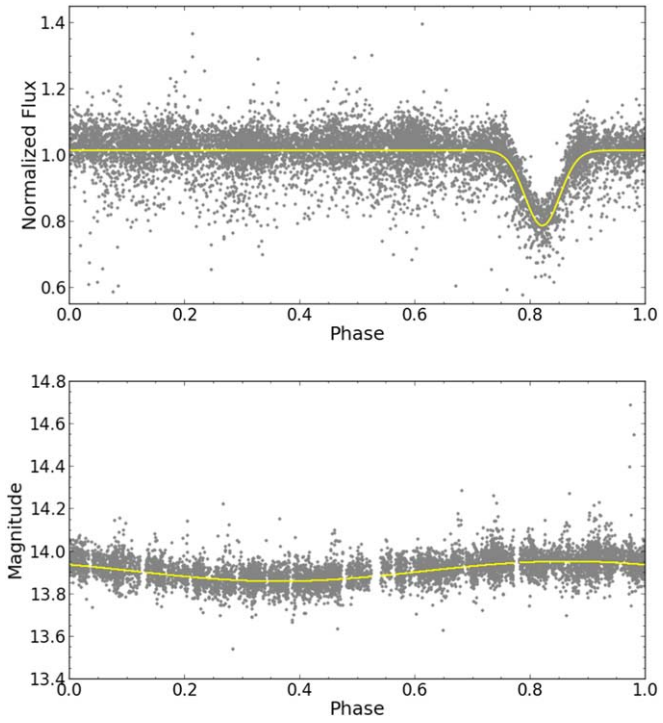

Figure 8. Top: eclipsing binary discovery EVRJ131324.31-792126.3 folded on its 33.7 hour period representative of hundreds of Evryscope variable discoveries. Gray points are two minute cadence and yellow is the best Gaussian fit to measure depth. Bottom: variable star discovery EVRJ131228.85-782429.2 folded on its 136.665 hour period representative of 100's of Evryscope variable discoveries. Gray points are 2-minute cadence and yellow is the best LS fit to measure amplitude.
(A color version of this figure is available in the online journal.)

are folded on the best period and fit with a Gaussian using the approximate phase and depth from the visual inspection plot as the prior. For the variable candidates, we use the best sinusoidal fit from the LS detection. Given the large number of candidates, fitting the light-curve amplitude consistently and automatically is key. An additional challenge is the degeneracy due to orbital angle, limb darkening, and orbital eccentricity. We find the Gaussian (for eclipsing binaries) and best sinusoidal fit from the LS detection (for variables) methods to be effective and efficient to measure the variability of the discoveries, while select targets with follow-up data can be fit with more complicated tools (see Section 4.3). Figure 8 shows an example eclipsing binary and variable star fit.

4.2. Identification Spectra

For the discoveries with potential low-mass secondaries, we compare the SOAR ID spectra to ESO template spectra (available at www.eso.org), see Figure 9. After finding the closest matching spectra, we compare the results from the color differences classifier described in the previous section. Finally,

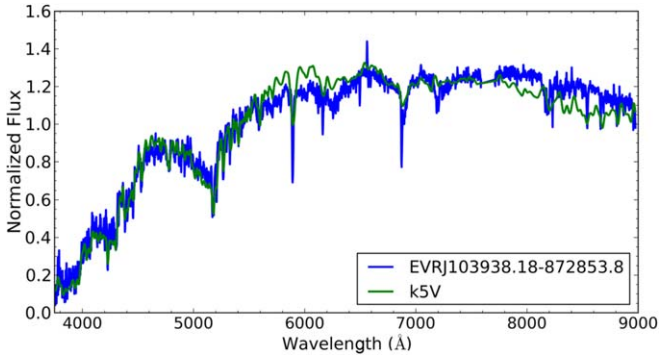

Figure 9. Example low-mass eclipsing binary discovery (EVRJ103938.18-872853.8) ID spectra taken with the Goodman Spectrograph on the 4.1 m SOAR telescope at CTIO, Chile. The green line is a K5V template from the ESO library.
(A color version of this figure is available in the online journal.)

we use the PyHammer (Covey et al. 2007) spectra fitting tool to confirm our fits. PyHammer uses empirical templates of known spectral types and performs a weighted least squares best fit to the input spectra and returns the estimated spectral type. For the the low-mass secondary eclipsing binaries, the results from the three methods are in agreement to within 1–2 in the luminosity class. The spectral types are shown in Table 8.

4.3. Radial Velocity—SOAR Data

We cross-correlate the SOAR spectra and measure the velocity shift throughout the period found in the Evryscope photometry. Using the color differences in Section 2.3, and the stellar type, radii, and mass profiles from Pecaut & Mamajek (2013), we derive functions (using 1D interpolation) to estimate the primary radius and mass. The secondary radius and mass are then determined using Keplarian/Newtonian calculations described in the following section. For this step, we assume a circular orbit, zero inclination angle, and no limb darkening. We run a Monte Carlo (MC) simulation to estimate the radius and mass ranges. Due to the simplifying zero-inclination angle assumption and the uncertainty in the SOAR RV measurements, our mass calculations for the secondaries are lower limits. More detailed modeling will be addressed in future work. We discuss our final solutions in Section 4.7. The results are listed in Table 8 and plots of the photometric and radial velocity light curves are shown in the appendix.

4.3.1. Secondary Mass and Radius Determination

Photometry: From visual inspection of the candidate light curves, an initial guess is made for the transit phase and depth and fit with a Gaussian (Figure 10). The data is fit with a least squares minimization using scipy to measure the amplitude and phase.

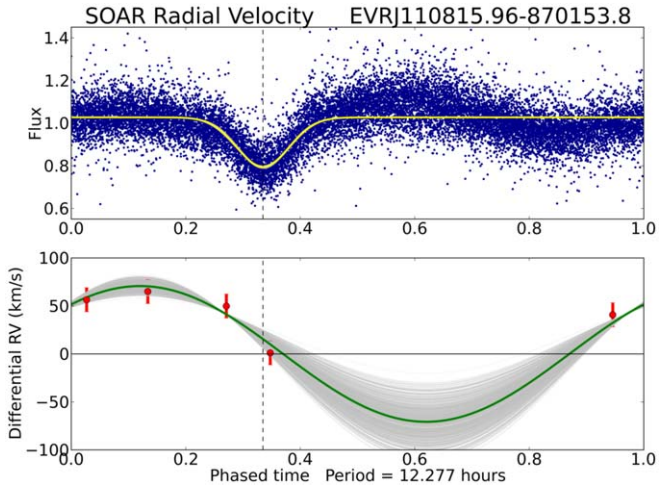

Figure 10. EVRJ110815.96-870153.8 K-dwarf eclipsing binary eclipse and radial velocity fit. Top: The best fit (yellow) to the Evryscope photometry using a Gaussian with an initial guess to measure the depth and determine secondary radius. Bottom: The best fit (green) to the SOAR RV data (red points) using a sine curve with an initial guess to measure the velocity and determine the secondary mass. The silver lines are the MC simulation to determine the best fit and error range.
(A color version of this figure is available in the online journal.)

Radial velocity: An initial sine curve fit is made using a guess for the amplitude and zero point, while the phase and period are controlled by the transit time and the period found in the photometric light curve (Figure 10). The amplitude and zero point are used as inputs to a sine fitting function that uses a sine curve with a fixed phase and period. The function fits the data with a least squares fit; this is the gold line and it returns an RV of 56 km/s for target EVRJ110815.96-870153.8. This assumes a circular orbit and edge on geometry. We leave more detailed analysis with additional variables to future work.

4.3.2. MC Best Fit of Mass and Radius

Using the methods described in the previous section, we perform a Monte Carlo simulation (as described in Press et al. 2007) to determine the best fit and distribution of the primary and secondary mass and radius.

From the Evryscope photometry, we use a bootstrap technique to leverage the very large number of epochs. We randomly choose half of the data points for each iteration with 5000 trials, and fit the data with a least squares minimization for each iteration. We also vary the radius of the primary for each trial by the range in (Pecaut & Mamajek 2013) (spanning $+/-1$ in numeric class). From the radial velocity data, we choose a random number in the error bar range of each of the data points (red) and fit the best sine curve (the silver curves) shown in Figure 10. We vary the mass of the primary for each trial by the error range in the estimated mass. The propagated results are shown in Figure 11.

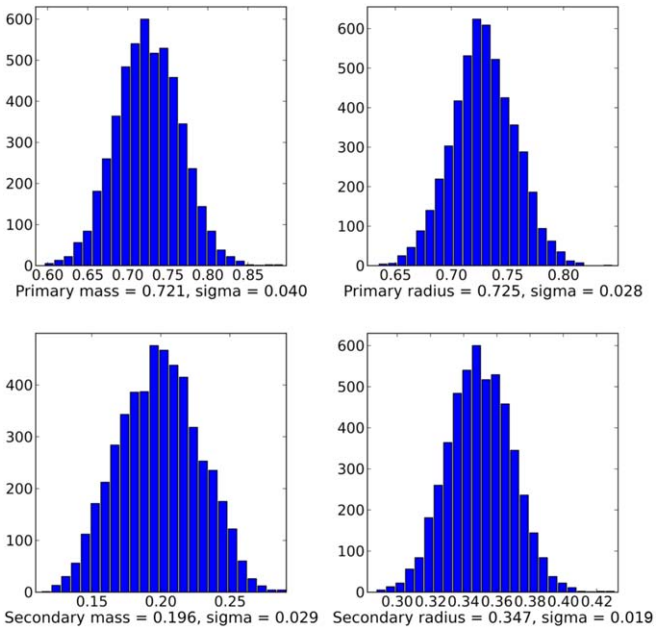

Figure 11. Primary and secondary mass and radius determined from our MC simulation. The top panels are the mass and radius of the primary in solar units, the bottom panels are the mass and radius of the secondary. The *y*-axis is the counts from the MC simulation totaling 5000 trials.
(A color version of this figure is available in the online journal.)

4.4. Search Statistics

Sorting by BLS sigma power and choosing only the top candidates greater than 10σ narrows the candidates to 5.6% (9104/163,584) of the filtered list. Visual inspection yields 7.3% (649/9104) actual variables from the BLS 10σ power list. The fraction of all discoveries to all searched is .40% (649/163,584). The false positive BLS rate is 5.2% (8455/163,584). Of 649 total variables detected, 346 are known in VSX. The total known periodic variables listed in VSX for the same sky area as the Evryscope Polar Search is 1928, giving a return of 17.9% (346/1928). There are 1050 known variables in the widest period ranges (3–720 hours) we searched, giving 33.0% return. There are 858 known variables in the period ranges (3–240 hours) we searched with BLS, giving 40.3% return. We add 303 new variables or 29% to the known variables in the region.

4.5. Eclipsing Binaries and Variables—Distribution of Results

Histograms of the eclipsing binary discoveries are shown in Figure 12. We discovered a total of 168 eclipsing binaries; most periods found are 75 hours or less, and most amplitudes found are 5%–25%. The results of the variables are shown in Figure 13, we found 135 total and most are smaller amplitudes and shorter periods.

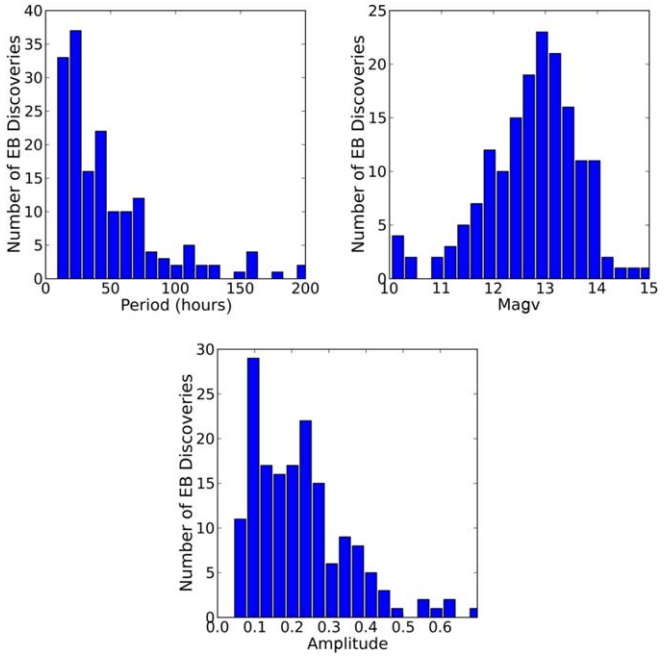

Figure 12. Histogram plots summarizing the eclipsing binary discovery results. We are sensitive to periods of several hundred hours and a large fraction of our discoveries are greater than 10% amplitude.
(A color version of this figure is available in the online journal.)

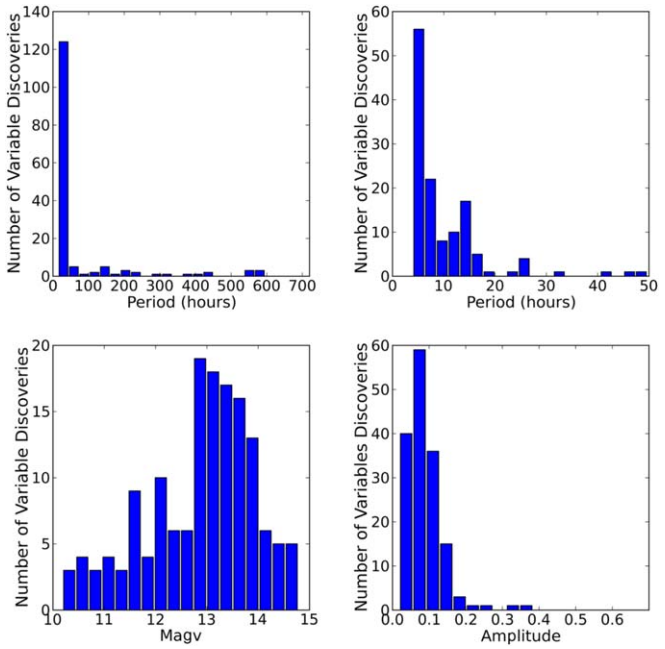

Figure 13. Histogram plots summarizing the variable discovery results. A larger fraction of the variable star discoveries are small amplitude and short period.
(A color version of this figure is available in the online journal.)

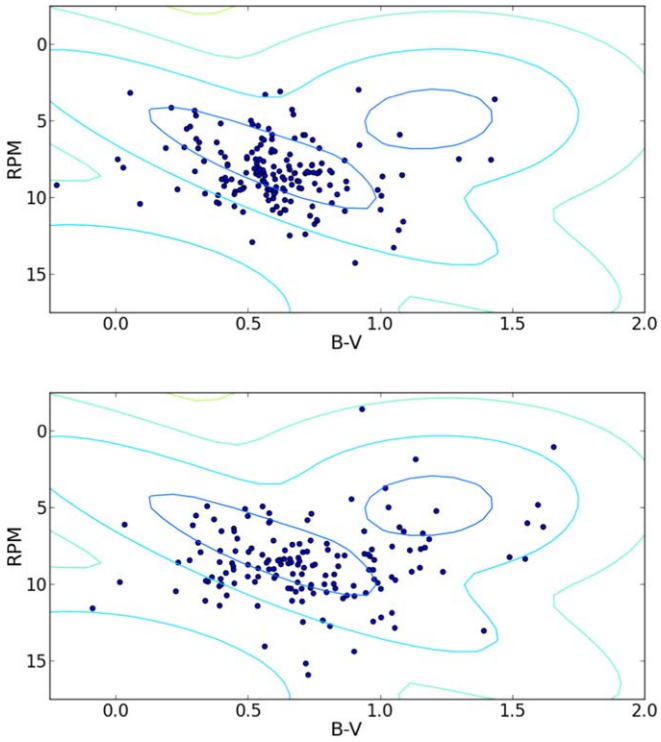

Figure 14. Classification results of the eclipsing binary and variable discoveries—Negative-log likelihood plot-lines 1, 1.7, 2.8 shown. Top: eclipsing binaries. Bottom: variables.
(A color version of this figure is available in the online journal.)

4.6. Classification

The discovery classification results are shown in Figure 14. We find 267 are main sequence, 34 are giants, and two are not classified. Spectral type G is the most common, with the spectral types shown in Table 6. We find more giant variables (24) than giant eclipsers (10) as shown in Figure 14. Also shown are the discoveries by star size and spectral type compared to total targets searched (Table 7).

4.7. Eclipsing Binaries with Low-mass Secondaries

We identified seven of the eclipsing binary discoveries as hosting potential low-mass secondaries and found that four are less than .25 solar mass. Three of the systems are fully eclipsing binaries (p = 12.3 to 25.9 hours) with dwarf primaries (SpT_p = G5V, K4V, K5V) and M-dwarf secondaries (mass = .06–.20 $M_\odot$). The other three systems are grazing eclipses with (p = 20.8 to 137.1 hours) with dwarf primaries (SpT_p = G8V, K2V, K7V), M-dwarf secondaries (mass = .24–.37 $M_\odot$) and minimum radii (r = .20 to .26 $r_\odot$). Table 8 presents a list of all low-mass secondary targets. Also

Table 6
Classification Discovery Results: Spectral Type

Classifier Spectral Type	Number of Discoveries	Percent
B	2	0.7
A	14	4.6
F	89	29.4
G	109	36.0
K	76	25.1
M	11	3.6
None	2	0.7
Total	303	100

Table 7
Classification Discovery Results, Compared with Total Searched

Classification	Total Searched	Number of Discoveries	Percent
MS	114585	267	0.23
Giant	40775	34	0.08
HSD	335	0	0.00
WD	21	0	0.00
O	20	0	0.00
B	331	2	0.60
A	4110	14	0.34
F	26102	89	0.34
G	49560	109	0.22
K	60964	76	0.12
M	14629	11	0.08

included is a likely visual binary EVRJ114225.51-793121.0 (separated in SOAR observations) and EVRJ211905.47-865829.3 a grazing EB with nearly identical primary and secondaries.

5. Summary

The Evryscope was deployed to CTIO in May 2015 and has been operational since that time. We conducted a variability search of the southern polar area using the first six months of available data and by selecting the brighter stars ($m_v < 14.5$) and limiting the declination range ($-75°$ to $-90°$). We sorted by detection power and visually searched the top 5% for variability. We recovered 346 known variables and discovered 303 new variables, including 168 eclipsing binaries six of which we identify as low-mass (.06–.37 $M_\odot$) secondaries with K-dwarf primaries. We encourage the community to follow-up further on these targets. We measured amplitudes, periods, and variability type and provide a catalog of all discoveries in the appendices.

This research was supported by the NSF CAREER grant AST-1555175 and the Research Corporation Scialog grants 23782 and 23822. H.C. is supported by the NSFGRF grant DGE-1144081. B.B. is supported by the NSF grant AST-1812874. O.F. and D.d.S. acknowledge support by the Spanish Ministerio de Economía y Competitividad (MINECO/FEDER, UE) under grants AYA2013-47447-C3-1-P, AYA2016-76012-C3-1-P, MDM-2014-0369 of ICCUB (Unidad de Excelencia 'María de Maeztu'). The Evryscope was constructed under NSF/ATI grant AST-1407589.

Appendix A
List of Eclipsing Binary Discoveries with Low-mass Secondaries

Eclipsing binaries with low-mass secondaries from the survey are shown here.

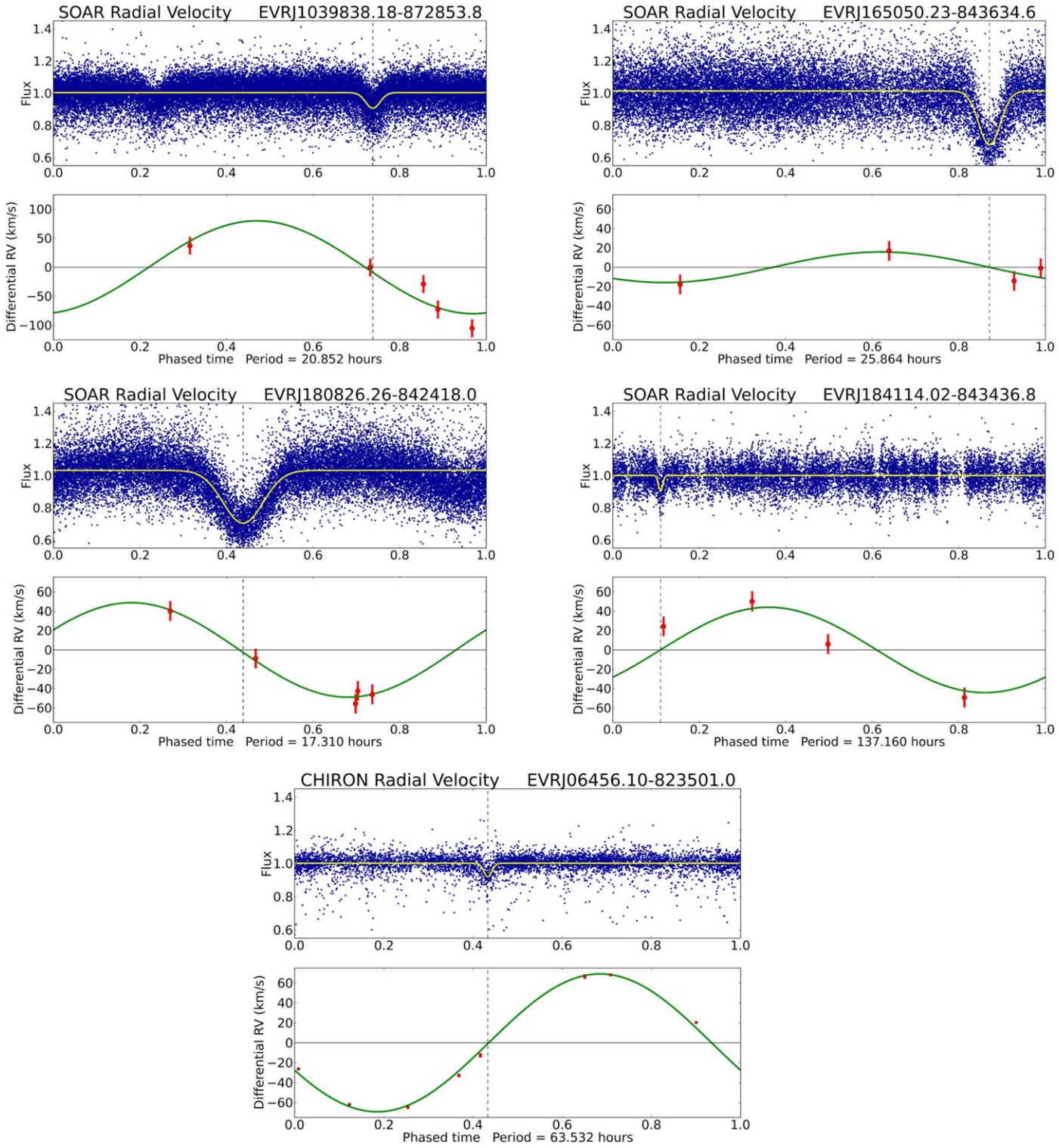

Figure 15. Low-mass secondary discoveries. Top panels are the Evryscope light curves with the best transit fit. Bottom panels are the SOAR RV points (red) with the best sinusoidal fit. Primary and secondary mass and radius values are shown in Table 2.
(A color version of this figure is available in the online journal.)

Table 8
Eclipsing Binary Discoveries with Low-mass Secondaries

ESID	R.A. (J2000)	Decl. (J2000)	M_v	RPM	B-V	Sptp	SOAR	Period (hours)	mp $M_\odot$	+/−	rp $R_\odot$	+/−	ms $M_\odot$	+/−	rs $R_\odot$	+/−
EVRJ06456.10-823501.0	101.2754	−82.5836	11.80	8.19	1.12	G9V	G8V	63.53	0.90	.04	.876	.059	.37	.02	.26	.01
EVRJ103938.18-872853.8	159.9091	−87.4816	13.78	12.09	1.07	K6V	K7V	20.85	0.63	.04	.655	.037	.24	.02	.20	.01
EVRJ110815.96-870153.8	167.0665	−87.0316	12.68	9.77	0.84	K3V	K4V	12.28	0.72	.04	.725	.028	.20	.03	.35	.02
EVRJ165050.23-843634.6	252.7093	−84.6096	13.84	11.54	1.09	K4V	K5V	25.86	0.68	.05	.699	.037	.06	.01	.40	.02
EVRJ180826.26-842418.0	272.1094	−84.405	13.51	9.81	0.57	G6V	G5V	17.31	0.98	.01	.983	.043	.19	.01	.56	.01
EVRJ184114.02-843436.8	280.3084	−84.5769	13.34	10.19	0.91	K3V	K2V	137.16	0.78	.07	.764	.052	.28	.03	.24	.02

Note. Columns 1–4 are identification numbers, right ascension, declination, and magnitude. Columns 5–6 are the reduced proper motion (RPM), color difference (B-V), which we use to estimate the star size and spectral type (see Section 4.2.1). Columns 7–8 are the spectral type from the classifier and from the SOAR ID spectra. Column 9 is the period found in hours. Columns 10–17 are the mass of the primary and secondary derived from SOAR radial velocity, along with the 1σ error.

Table 9
Peculiar Eclipsing Binary Discoveries

ESID	R.A. (J2000)	Decl. (J2000)	M_v	RPM	B-V	Sptp	SOAR	Period	Note
EVRJ053513.22-774248.2	83.8051	−77.7134	12.05	9.00	1.03	K1V	G7V	50.96	Nearly identical primary and secondary
EVRJ114225.51-793121.0	175.6063	−79.5225	12.81	12.66	0.95	K3V	⋯	91.82	Visual Double in SOAR image
EVRJ211905.47-865829.3	319.7728	−86.9748	13.97	10.60	0.95	K6V	K5V	18.61	Nearly identical primary and secondary

Note. Columns 1–4 are identification numbers, right ascension, declination, and magnitude. Columns 5–6 are the reduced proper motion (RPM), color difference (B-V), which we use to estimate the star size and spectral type (see Section 4.2.1). Columns 7–8 are the spectral type from the classifier and from the SOAR ID spectra. Column 9 is the period found in hours.

Appendix B
List of All Variable Discoveries

Variables from the survey are shown here.

Table 10
Variable Star Discoveries

ESID	APASSID	R.A. (J2000)	Decl. (J2000)	M_v	RPM	B-V	Size	Spec	Period (hours)	Amplitude (Δ mag)
EVRJ000411.09-862200.5	36032704	1.0462	−86.3668	12.91	10.27	1.00	ms	K3V	3.7893	0.048
EVRJ004033.86-852556.3	36034219	10.1411	−85.4323	13.88	8.56	0.57	ms	G0V	11.9673	0.108
EVRJ010354.79-845024.4	36034985	15.9783	−84.8401	13.07	9.70	1.06	ms	K6V	66.0947	0.067
EVRJ010428.68-752821.7	36397673	16.1195	−75.4727	12.74	8.80	0.44	ms	F1V	4.4661	0.056
EVRJ010628.13-821135.5	36109108	16.6172	−82.1932	10.79	6.12	0.29	ms	A1V	11.5043	0.021
EVRJ011610.92-853620.5	36033299	19.0455	−85.6057	13.56	9.95	0.82	ms	G8V	4.0396	0.061
EVRJ013112.26-754727.2	36147371	22.8011	−75.7909	12.69	7.03	1.18	giant	K6	565.2369	0.057
EVRJ014744.62-750722.8	36149487	26.9359	−75.1230	13.43	9.75	0.34	ms	F2V	7.9793	0.022
EVRJ015507.25-842951.4	36036929	28.7802	−84.4976	12.03	1.82	1.13	giant	K4	207.4862	0.048
EVRJ020014.59-824041.2	36042924	30.0608	−82.6781	13.68	11.05	0.66	ms	F3V	3.8633	0.048
EVRJ020627.84-854259.4	36017206	31.6160	−85.7165	13.10	5.95	0.58	ms	F1V	4.2580	0.049
EVRJ021301.18-850613.7	36035338	33.2549	−85.1038	14.18	8.74	0.74	ms	F9V	14.5239	0.044
EVRJ022525.78-871212.6	36013743	36.3574	−87.2035	13.72	5.85	0.58	ms	F9V	5.4833	0.128
EVRJ023633.12-841813.7	36036143	39.1380	−84.3038	12.99	8.31	1.55	giant	M	3.0339	0.026
EVRJ024105.09-852056.8	36017369	40.2712	−85.3491	10.84	6.65	1.16	giant	M0	383.3562	0.031
EVRJ031048.98-774610.2	36092849	47.7041	−77.7695	13.43	9.01	0.44	ms	F1V	5.5437	0.107
EVRJ031437.25-812625.4	36050275	48.6552	−81.4404	11.83	10.24	0.65	ms	G6V	22.5360	0.038
EVRJ032340.58-833811.4	36027122	50.9191	−83.6365	11.73	5.37	0.74	giant	G8	3.6540	0.115
EVRJ032442.50-780853.9	36092101	51.1771	−78.1483	11.38	6.51	0.45	ms	F5V	4.6764	0.022
EVRJ034027.74-771628.9	36093941	55.1156	−77.2747	11.26	8.02	0.95	ms	K4V	527.5689	0.041
EVRJ035648.91-810628.4	36049584	59.2038	−81.1079	12.66	8.40	0.28	ms	A9V	10.7653	0.035
EVRJ040145.72-794920.3	36086352	60.4405	−79.8223	13.50	7.80	0.45	ms	F1V	4.3002	0.063
EVRJ041253.57-812919.7	36066969	63.2232	−81.4888	13.91	12.69	0.81	ms	G	5.5612	0.061
EVRJ041719.75-803105.5	36068185	64.3323	−80.5182	11.38	6.23	1.61	giant	M	583.9396	0.066
EVRJ042003.70-803034.9	36068172	65.0154	−80.5097	12.35	5.20	1.21	giant	M0	423.7755	0.158
EVRJ042008.90-790539.1	36088224	65.0371	−79.0942	13.38	8.98	0.58	ms	G2V	5.0229	0.085
EVRJ044109.58-774556.5	36081406	70.2899	−77.7657	10.19	5.99	1.55	giant	M	426.2952	0.046
EVRJ044130.53-761227.0	36099120	70.3772	−76.2075	13.13	8.14	0.96	ms	K3V	3.3209	0.065
EVRJ044735.35-775219.9	36081082	71.8973	−77.8722	11.30	8.69	0.50	ms	G1V	3.3276	0.026
EVRJ050012.05-811743.4	36061636	75.0502	−81.2954	12.48	8.09	0.86	ms	G9V	3.4901	0.076
EVRJ051213.46-761626.0	36201329	78.0561	−76.2739	12.99	9.39	0.60	ms	G1V	6.3173	0.074
EVRJ051707.51-851934.3	36019388	79.2813	−85.3262	14.56	11.54	−0.09	ms	F0	17.4600	0.138
EVRJ053531.56-792945.6	36073410	83.8815	−79.4960	13.45	10.57	0.75	ms	K0V	4.8621	0.061
EVRJ053802.81-775651.0	36077655	84.5117	−77.9475	12.60	9.47	0.50	ms	G0V	6.8030	0.048
EVRJ053857.96-840027.0	36021952	84.7415	−84.0075	13.18	8.45	0.69	ms	K2V	3.7923	0.120
EVRJ053921.36-823350.0	36059589	84.8390	−82.5639	11.37	7.67	1.15	giant	K5	294.1877	0.042
EVRJ055148.46-761552.6	36198063	87.9519	−76.2646	11.87	4.41	0.89	giant	K4	98.4013	0.048

Table 10
(Continued)

ESID	APASSID	R.A. (J2000)	Decl. (J2000)	M_v	RPM	B-V	Size	Spec	Period (hours)	Amplitude (Δ mag)
EVRJ055157.14-810831.9	36062821	87.9881	−81.1422	12.74	9.85	0.69	ms	F5V	4.9623	0.208
EVRJ055856.16-785946.3	36075508	89.7340	−78.9962	13.06	9.65	0.98	ms	K4V	3.1286	0.078
EVRJ060627.19-841156.4	37958830	91.6133	−84.1990	14.67	9.83	0.01	ms	F0	6.8412	0.142
EVRJ061823.95-780812.1	38123485	94.5998	−78.1367	10.11	1.02	1.65	giant	M	544.3723	0.064
EVRJ062714.64-794039.0	38117589	96.8110	−79.6775	13.19	8.31	0.66	ms	G2V	5.1073	0.080
EVRJ064843.42-793349.3	38116489	102.1809	−79.5637	13.01	9.15	1.24	giant	M1	534.1532	0.095
EVRJ070444.11-752812.7	39299363	106.1838	−75.4702	13.39	8.69	0.69	ms	G6V	4.9315	0.098
EVRJ070553.98-813347.5	38085679	106.4749	−81.5632	13.28	12.32	0.78	ms	G	208.1137	0.080
EVRJ070751.77-861600.8	37950806	106.9657	−86.2669	13.88	10.26	0.70	ms	G6V	4.4384	0.137
EVRJ071040.15-854213.0	37951603	107.6673	−85.7036	13.28	10.46	0.68	ms	G7V	14.0116	0.042
EVRJ071054.50-775214.5	38120922	107.7271	−77.8707	12.75	8.38	0.98	ms	K6V	119.7744	0.061
EVRJ072150.93-814705.3	38084504	110.4622	−81.7848	12.48	3.69	1.02	giant	K4	569.9960	0.073
EVRJ072411.33-865020.0	37932897	111.0472	−86.8389	12.06	7.72	0.80	ms	G8V	3.8106	0.036
EVRJ074325.18-780127.5	38108272	115.8549	−78.0243	11.58	7.86	0.50	ms	F7V	3.3874	0.029
EVRJ080401.49-824005.9	37961948	121.0062	−82.6683	11.55	7.70	0.97	giant	K6	4.2669	0.028
EVRJ083403.17-811922.4	37975768	128.5132	−81.3229	13.54	−1.46	0.93	giant	K4	5.1269	0.047
EVRJ084757.72-781627.1	38100581	131.9905	−78.2742	13.17	12.13	1.00	ms	K4V	266.6131	0.064
EVRJ085910.42-813844.9	37967866	134.7934	−81.6458	13.69	9.23	0.41	ms	A4V	6.5406	0.073
EVRJ090816.25-840058.0	37945248	137.0677	−84.0161	13.73	9.56	0.60	ms	G1V	4.1451	0.159
EVRJ092130.62-780552.1	38047442	140.3776	−78.0978	12.06	7.58	1.17	giant	K8	14.2823	0.036
EVRJ092934.58-883002.5	37925391	142.3941	−88.5007	12.70	11.83	1.04	ms	K4V	14.9276	0.072
EVRJ094546.82-845901.7	37943780	146.4451	−84.9838	11.40	4.88	0.34	ms	F4V	10.5364	0.023
EVRJ094914.47-765810.9	38050263	147.3103	−76.9697	11.94	7.38	0.67	ms	G1V	4.7866	0.047
EVRJ095103.38-775148.6	38042145	147.7641	−77.8635	12.64	8.52	0.39	ms	A9V	3.3413	0.052
EVRJ103805.95-823919.8	37947694	159.5248	−82.6555	12.25	9.15	1.12	ms	K5V	188.7851	0.037
EVRJ103843.68-841342.6	37941994	159.6820	−84.2285	14.34	9.32	0.82	ms	K1V	3.4514	0.095
EVRJ104338.88-812945.6	37997111	160.9120	−81.4960	13.10	12.81	1.05	ms	K	9.2306	0.071
EVRJ104928.30-840709.1	37941961	162.3679	−84.1192	14.41	10.25	0.66	ms	G5V	4.3652	0.071
EVRJ110736.10-801214.8	37995054	166.9004	−80.2041	13.20	8.60	0.65	ms	G6V	5.2520	0.103
EVRJ112926.09-790251.7	38014623	172.3587	−79.0477	12.82	10.01	0.74	ms	K3V	3.2616	0.032
EVRJ113221.60-773934.2	38021372	173.0900	−77.6595	12.62	7.52	0.64	ms	F6V	2.2946	0.089
EVRJ113648.94-770820.8	38274528	174.2039	−77.1391	13.07	10.70	0.87	ms	K2V	40.9161	0.049
EVRJ113950.33-823313.7	37986809	174.9597	−82.5538	12.70	8.23	0.69	ms	G9V	12.2413	0.045
EVRJ121247.35-782517.8	47439342	183.1973	−78.4216	12.77	8.67	0.75	ms	G8V	7.1346	0.071
EVRJ124042.22-852021.1	47199888	190.1759	−85.3392	12.33	7.11	0.73	ms	K1V	51.6660	0.093
EVRJ124521.96-772053.5	47445563	191.3415	−77.3482	13.16	8.11	0.84	ms	G8V	5.0777	0.089
EVRJ124614.88-851715.4	47199917	191.5620	−85.2876	13.75	12.43	0.71	ms	G8V	3.6741	0.109
EVRJ124711.98-784313.8	−-	191.7999	−78.7205	−-	−-	−-	−-	−-	4.0535	0.100
EVRJ125757.58-773925.9	47442656	194.4899	−77.6572	12.88	9.03	0.97	ms	K2V	13.6397	0.065
EVRJ130148.17-831417.9	47209493	195.4507	−83.2383	12.92	8.20	1.49	giant	M3	121.8445	0.068
EVRJ130916.78-775637.7	47433337	197.3199	−77.9438	13.61	9.88	0.99	ms	K4V	7.8242	0.153
EVRJ131216.99-803701.6	47370231	198.0708	−80.6171	11.08	5.79	0.72	ms	G9V	7.9778	0.008
EVRJ131228.85-782429.2	−-	198.1202	−78.4081	−-	−-	−-	−-	−-	136.7678	0.047
EVRJ131248.91-794104.9	47374655	198.2038	−79.6847	10.48	7.50	1.04	giant	K4	5.5061	0.015
EVRJ134036.82-810805.3	47361846	205.1534	−81.1348	13.08	10.74	0.90	ms	K0V	3.4605	0.038
EVRJ134909.43-795116.2	47384377	207.2893	−79.8545	12.69	9.02	0.96	ms	K1V	4.4504	0.032
EVRJ135636.96-852904.9	47198519	209.1540	−85.4847	13.04	9.29	0.67	ms	G8V	5.5375	0.039
EVRJ135847.35-753616.9	47466750	209.6973	−75.6047	12.64	4.90	0.55	ms	F8V	13.0043	0.081
EVRJ135948.38-773732.9	47408549	209.9516	−77.6258	12.25	7.12	0.59	ms	G0V	6.4798	0.063
EVRJ142647.47-774451.4	47396223	216.6978	−77.7476	13.36	11.36	0.39	ms	F0	3.0402	0.110
EVRJ143601.82-832825.3	47204308	219.0076	−83.4737	13.62	9.82	0.52	ms	F2V	6.8145	0.117
EVRJ150519.75-753054.0	47509935	226.3323	−75.5150	10.53	4.96	1.03	giant	K3	6.7618	0.036
EVRJ151320.26-833642.1	47215664	228.3344	−83.6117	11.52	7.98	0.94	ms	K3V	202.2009	0.027
EVRJ152213.03-850853.2	47177228	230.5543	−85.1481	12.59	7.32	0.80	ms	K0V	44.3809	0.081
EVRJ152422.85-765355.7	47316062	231.0952	−76.8988	10.58	5.74	0.37	ms	A7V	3.3395	0.042
EVRJ154618.22-824405.3	47194254	236.5759	−82.7348	13.77	11.09	0.70	ms	F6V	4.5592	0.091
EVRJ155137.18-824810.8	47194265	237.9049	−82.8030	12.70	8.58	0.44	ms	F5V	8.0204	0.052

Table 10
(Continued)

ESID	APASSID	R.A. (J2000)	Decl. (J2000)	M_v	RPM	B-V	Size	Spec	Period (hours)	Amplitude (Δ mag)
EVRJ155320.98-824654.8	47193653	238.3374	−82.7819	12.98	5.06	0.49	ms	F8V	10.0283	0.044
EVRJ155645.07-802819.2	47288797	239.1878	−80.4720	11.75	6.08	0.03	ms	B9V	116.9858	0.032
EVRJ155942.19-824514.8	47193923	239.9258	−82.7541	12.12	5.33	0.58	ms	G0V	14.6855	0.038
EVRJ162259.47-805820.3	47254401	245.7478	−80.9723	11.73	8.04	0.55	ms	F1V	4.8019	0.048
EVRJ162554.07-854342.2	47181390	246.4753	−85.7284	13.37	11.38	0.53	ms	F5V	5.0865	0.083
EVRJ163031.56-834849.7	47191010	247.6315	−83.8138	13.35	8.31	0.63	ms	G0V	12.2352	0.089
EVRJ163252.27-832748.2	47191300	248.2178	−83.4634	12.51	6.51	0.94	giant	K6	150.4504	0.092
EVRJ163852.99-843744.0	47182121	249.7208	−84.6289	13.21	10.49	0.80	ms	K2V	32.2767	0.048
EVRJ165216.22-825416.6	47186184	253.0676	−82.9046	13.94	9.91	0.45	ms	F8V	15.1777	0.367
EVRJ165457.58-775615.7	47277017	253.7399	−77.9377	12.87	5.49	0.30	ms	F1V	7.4973	0.069
EVRJ171344.76-825649.9	47243917	258.4365	−82.9472	13.44	7.62	0.51	ms	F3V	5.2027	0.075
EVRJ171929.86-800819.0	47250893	259.8744	−80.1386	12.85	8.54	0.66	ms	F3V	4.5325	0.071
EVRJ171939.84-852016.4	47180802	259.9160	−85.3379	14.67	13.00	1.39	ms	K6V	3.2852	0.072
EVRJ172044.45-811413.2	47249474	260.1852	−81.2370	10.80	7.87	0.71	ms	G1V	12.2459	0.019
EVRJ173256.64-833249.9	47242117	263.2360	−83.5472	14.11	10.70	0.42	ms	F8V	7.1155	0.135
EVRJ173854.53-825617.2	47243150	264.7272	−82.9381	13.40	11.05	0.34	ms	F3	6.2448	0.087
EVRJ174904.92-853647.9	47180335	267.2705	−85.6133	13.89	7.33	0.69	ms	G1V	4.3006	0.093
EVRJ175053.26-794941.5	47264410	267.7219	−79.8282	11.96	8.79	0.84	ms	K0V	134.4649	0.051
EVRJ175230.22-785048.8	47268452	268.1259	−78.8469	12.01	7.88	0.32	ms	F1V	8.3917	0.041
EVRJ175340.68-753831.9	47710653	268.4195	−75.6422	12.35	7.83	0.72	ms	G8V	5.0187	0.089
EVRJ175347.33-854135.5	47180309	268.4472	−85.6932	12.81	8.92	0.54	ms	F9V	4.4685	0.051
EVRJ180742.10-824651.6	57161419	271.9254	−82.7810	14.02	10.10	0.39	ms	F0V	7.0683	0.224
EVRJ181807.06-800525.4	57185282	274.5294	−80.0904	11.04	4.80	1.59	giant	M	370.8165	0.025
EVRJ182044.62-754759.6	57415585	275.1859	−75.7999	11.50	5.52	0.50	ms	F7V	3.4102	0.026
EVRJ182608.74-864925.3	57090707	276.5364	−86.8237	14.41	10.07	0.90	ms	K2V	4.2908	0.130
EVRJ183802.93-811827.4	57166241	279.5122	−81.3076	10.90	10.24	0.83	ms	K1V	48.6808	0.051
EVRJ192029.45-860534.4	57091324	290.1227	−86.0929	13.27	9.80	0.35	ms	A7V	6.0642	0.025
EVRJ195449.01-840216.4	57097667	298.7042	−84.0379	12.73	10.22	0.73	ms	G9V	5.5082	0.063
EVRJ200551.67-820620.5	57105858	301.4653	−82.1057	13.63	8.88	0.71	ms	G9V	5.5203	0.087
EVRJ203404.49-871549.0	57072262	308.5187	−87.2636	13.87	9.50	0.36	ms	F1V	4.8050	0.095
EVRJ204931.97-845034.4	57076995	312.3832	−84.8429	14.21	15.14	0.72	ms	G	4.4090	0.078
EVRJ205037.49-774637.2	57175393	312.6562	−77.7770	11.00	6.99	0.46	ms	F8V	3.3040	0.023
EVRJ205225.92-855742.5	57074554	313.1080	−85.9618	14.07	12.40	0.97	ms	K3V	133.5587	0.062
EVRJ205802.14-793349.7	57118550	314.5089	−79.5638	12.97	8.41	0.61	ms	F7V	6.2271	0.048
EVRJ210729.26-763906.5	57215979	316.8719	−76.6518	13.58	10.43	0.23	ms	F3	4.7894	0.024
EVRJ210937.03-785828.2	57118801	317.4043	−78.9745	12.99	6.25	1.07	giant	K4	180.8028	0.051
EVRJ213403.58-865953.5	57070601	323.5149	−86.9982	12.69	8.97	0.60	ms	F9V	4.7182	0.082
EVRJ215744.06-790828.7	57141740	329.4336	−79.1413	13.51	7.75	1.11	giant	K5	10.6690	0.148
EVRJ220737.90-813510.0	57090539	331.9079	−81.5861	11.93	14.35	0.90	ms	G	14.9246	0.016
EVRJ223616.97-773616.2	57136977	339.0707	−77.6045	13.55	8.89	1.15	giant	K6	2074.7965	0.299
EVRJ235019.03-840248.8	57081420	357.5793	−84.0469	11.40	7.79	0.39	ms	F5V	5.8564	0.020

Note. Columns 1–5 are identification numbers, right ascension, declination, and magnitude. Columns 6–9 are the reduced proper motion (RPM), color difference (B-V), which we use to estimate the star size and spectral type (see Section 4.2.1). Columns 10 and 11 are the period found in hours, and the amplitude of the variability in magnitudes.

Table 11
Eclipsing Binary Discoveries

ESID	APASSID	R.A. (J2000)	Decl. (J2000)	M_v	RPM	B-V	Size	Spec	Period (hours)	Depth (fractional)
EVRJ002445.62-784031.1	36136315	6.1901	−78.6753	11.78	6.21	0.56	ms	G9V	109.3650	0.118
EVRJ004748.46-754942.6	36397363	11.9519	−75.8285	11.79	5.20	0.52	ms	F9V	157.4220	0.229
EVRJ005637.85-782127.0	36134521	14.1577	−78.3575	12.39	8.65	0.63	ms	G5V	74.0640	0.273
EVRJ010726.33-774753.2	36135199	16.8597	−77.7981	12.96	8.26	0.30	ms	A5V	15.7654	0.148
EVRJ012740.66-841645.1	36035232	21.9194	−84.2792	13.25	7.92	0.65	ms	G1V	20.0793	0.109
EVRJ013849.70-842426.6	36037250	24.7071	−84.4074	13.24	14.24	0.90	ms	K	198.5830	0.172
EVRJ014115.60-800737.9	36113485	25.3150	−80.1272	14.97	9.44	0.23	ms	G2V	22.1010	0.187
EVRJ023605.38-852430.6	36017318	39.0224	−85.4085	12.75	7.47	0.54	ms	F1V	118.7710	0.225
EVRJ024203.26-750224.0	36161150	40.5136	−75.0400	11.98	6.76	0.31	ms	F4V	30.9563	0.243
EVRJ024438.52-835122.7	36036709	41.1605	−83.8563	12.50	8.28	0.72	ms	G8V	25.9882	0.303
EVRJ030147.71-761211.5	36155585	45.4488	−76.2032	10.14	2.93	0.92	giant	K3	68.3947	0.065
EVRJ032000.70-760821.5	36156333	50.0029	−76.1393	13.15	10.03	0.59	ms	F9V	79.5734	0.202
EVRJ032206.70-752842.6	36157171	50.5279	−75.4785	12.91	9.86	1.00	ms	K4V	7.3698	0.147
EVRJ032355.42-783922.7	36091552	50.9809	−78.6563	11.40	8.26	0.62	ms	F8V	22.0561	0.215
EVRJ033317.16-792812.7	36087183	53.3215	−79.4702	13.30	9.82	0.38	ms	A8V	21.1649	0.095
EVRJ043634.42-863132.9	36012543	69.1434	−86.5258	14.30	11.43	0.76	ms	F1V	8.1408	0.221
EVRJ043913.51-855448.6	36019521	69.8063	−85.9135	10.23	8.34	0.82	ms	G3V	36.8604	0.054
EVRJ043932.02-794339.0	36070451	69.8834	−79.7275	11.53	6.84	0.59	ms	F9V	61.6244	0.117
EVRJ044501.22-771324.6	36081663	71.2551	−77.2235	11.33	10.78	0.59	ms	F9V	85.9685	0.217
EVRJ044545.98-770625.6	36081683	71.4416	−77.1071	13.16	4.63	0.30	ms	F1V	17.5505	0.387
EVRJ045203.19-853702.6	36019627	73.0133	−85.6174	12.49	10.39	0.09	ms	F9	30.2652	0.092
EVRJ045807.78-772037.7	36082386	74.5324	−77.3438	12.58	8.92	0.69	ms	G6V	38.1567	0.379
EVRJ050731.01-760919.8	36201646	76.8792	−76.1555	13.38	10.14	0.64	ms	G2V	10.7099	0.065
EVRJ052042.43-753131.8	36202184	80.1768	−75.5255	11.06	3.14	0.05	ms	A1V	64.8150	0.322
EVRJ053006.26-811232.4	36062995	82.5261	−81.2090	11.95	7.32	0.49	ms	F8V	45.1688	0.217
EVRJ053504.90-834045.5	36058479	83.7704	−83.6793	12.40	9.23	0.41	ms	F9V	35.7837	0.130
EVRJ053541.69-753728.6	36199669	83.9237	−75.6246	12.75	8.21	0.81	ms	K2V	31.2876	0.113
EVRJ054814.83-772912.5	36195270	87.0618	−77.4868	13.85	9.49	0.47	ms	G3V	17.3382	0.611
EVRJ055000.48-780018.7	36076437	87.5020	−78.0052	13.60	8.79	0.44	ms	G0V	22.1010	0.243
EVRJ055918.00-861604.1	36018864	89.8250	−86.2678	12.51	8.16	0.54	ms	G6V	16.0350	0.101
EVRJ060300.82-763227.2	39301921	90.7534	−76.5409	13.01	9.37	0.63	ms	G6V	35.3178	0.368
EVRJ060956.86-842635.9	37958393	92.4869	−84.4433	12.32	8.02	0.03	ms	F1	64.7228	0.106
EVRJ061730.58-853507.8	37952210	94.3774	−85.5855	13.76	9.17	−0.23	ms	A0	19.5420	0.064
EVRJ061942.89-872037.7	37932270	94.9287	−87.3438	12.77	8.30	0.53	ms	G0V	11.7925	0.176
EVRJ062614.11-812323.6	38088026	96.5588	−81.3899	12.84	9.76	0.45	ms	F8V	22.1397	0.057
EVRJ065136.84-775609.6	38124833	102.9035	−77.9360	11.32	4.24	0.66	giant	G5	154.2250	0.158
EVRJ065350.93-840014.0	37957964	103.4622	−84.0039	12.91	9.75	0.60	ms	K0V	45.7400	0.212
EVRJ065609.43-810853.5	38088326	104.0393	−81.1482	13.49	12.36	0.71	ms	K0V	13.4842	0.116
EVRJ070327.70-813323.4	38085967	105.8654	−81.5565	13.29	9.59	0.45	ms	A9V	22.2891	0.357
EVRJ071503.55-792949.6	38091930	108.7648	−79.4971	13.08	7.32	0.41	ms	G1V	35.9922	0.599
EVRJ071744.33-854505.4	37951607	109.4347	−85.7515	13.09	6.75	0.77	ms	K3V	101.6850	0.314
EVRJ071748.29-844104.6	37953026	109.4512	−84.6846	14.52	10.35	0.39	ms	G3V	7.6682	0.184
EVRJ071938.74-794442.4	38091354	109.9114	−79.7451	12.18	5.14	0.39	ms	F2V	20.8352	0.107
EVRJ072710.08-815757.2	38084205	111.7920	−81.9659	13.73	5.29	0.54	ms	G9V	41.0657	1.000
EVRJ073157.14-815943.4	38084148	112.9881	−81.9954	9.93	6.74	0.19	ms	F1V	60.0174	0.074
EVRJ074851.14-844938.3	37953692	117.2131	−84.8273	13.18	8.90	0.56	ms	F	23.3998	0.115
EVRJ075512.70-831036.1	37960834	118.8029	−83.1767	12.40	8.05	0.54	ms	F8V	68.9536	0.237
EVRJ080959.06-765721.2	38113121	122.4961	−76.9559	12.33	8.08	0.52	ms	F8V	109.3650	0.257
EVRJ082431.85-771708.5	38110818	126.1327	−77.2857	10.99	6.53	0.55	ms	G1V	46.0730	0.162
EVRJ083235.69-814208.3	37974452	128.1487	−81.7023	13.27	10.91	0.48	ms	G7V	22.5004	0.273
EVRJ083610.66-822751.1	37966550	129.0444	−82.4642	12.08	7.46	1.30	giant	K	15.4668	0.066
EVRJ084853.45-755536.1	38163662	132.2227	−75.9267	10.01	5.34	0.28	ms	F8V	59.1296	0.081
EVRJ085629.66-833101.6	37964619	134.1236	−83.5171	12.47	4.96	0.51	ms	F1V	59.1383	0.250
EVRJ090851.91-835702.5	37945252	137.2163	−83.9507	13.29	8.89	0.42	ms	F1V	10.8306	0.337
EVRJ091345.72-822820.3	37965615	138.4405	−82.4723	11.75	6.95	0.60	ms	G5V	43.7381	0.182
EVRJ092241.74-833802.0	37945406	140.6739	−83.6339	13.77	8.53	0.54	ms	G0V	4.4717	0.145
EVRJ093342.00-865534.0	37929506	143.4250	−86.9261	13.03	8.34	0.75	ms	G9V	106.1730	0.347
EVRJ093554.48-763543.8	38051623	143.9770	−76.5955	13.59	4.56	0.67	giant	F6	35.6159	0.248

Table 11
(Continued)

ESID	APASSID	R.A. (J2000)	Decl. (J2000)	M_v	RPM	B-V	Size	Spec	Period (hours)	Depth (fractional)
EVRJ093619.37-811153.2	37970069	144.0807	−81.1981	13.13	10.33	0.82	ms	K1V	129.2850	0.239
EVRJ094641.04-781309.8	38041815	146.6710	−78.2194	13.00	7.60	0.56	ms	G2V	33.1735	0.231
EVRJ095515.41-830705.9	37948497	148.8142	−83.1183	12.88	9.48	0.59	ms	G5V	151.7600	0.345
EVRJ100205.04-814503.2	37950302	150.5210	−81.7509	12.79	6.15	0.30	ms	F5V	67.4233	0.196
EVRJ100426.40-803846.0	38032563	151.1100	−80.6461	13.09	7.01	0.59	ms	F6V	28.3768	0.095
EVRJ100649.61-801046.9	38033725	151.7067	−80.1797	12.65	12.88	0.51	ms	F4	44.7694	0.205
EVRJ101423.47-774932.5	38040775	153.5978	−77.8257	13.29	13.24	1.05	ms	K	35.1543	0.083
EVRJ103443.51-775813.1	38026295	158.6813	−77.9703	10.88	10.79	0.64	ms	G4V	20.9396	0.029
EVRJ105421.24-782234.7	38024299	163.5885	−78.3763	12.41	10.76	1.00	ms	K6V	20.3265	0.081
EVRJ105445.86-785351.4	38023795	163.6911	−78.8976	12.69	10.56	0.61	ms	G9V	62.0270	0.169
EVRJ110105.30-864038.6	37928838	165.2721	−86.6774	13.73	9.45	0.58	ms	G7V	42.5378	0.096
EVRJ110815.96-870153.8	37928658	167.0665	−87.0316	12.68	9.77	0.84	ms	K3V	12.2767	0.230
EVRJ111244.66-830219.7	37987113	168.1861	−83.0388	13.18	7.43	0.49	ms	G7V	17.3342	0.277
EVRJ111447.02-811836.7	37992322	168.6959	−81.3102	12.41	10.99	0.62	ms	G6V	35.0246	0.171
EVRJ112755.49-842109.7	37940976	171.9812	−84.3527	13.81	9.72	0.34	ms	F8V	8.4533	0.252
EVRJ114502.30-771447.0	38272180	176.2596	−77.2464	12.29	7.73	0.78	ms	G4V	39.2816	0.209
EVRJ114706.02-835834.7	37940896	176.7751	−83.9763	12.90	9.39	0.87	ms	K3V	54.3094	0.091
EVRJ120501.68-852738.9	47205316	181.2570	−85.4608	12.73	9.41	0.48	ms	F6V	103.6910	0.144
EVRJ120856.86-770450.9	48482910	182.2369	−77.0808	13.21	6.55	0.92	giant	K2	40.7350	0.275
EVRJ122230.55-772324.4	48480777	185.6273	−77.3901	11.60	8.26	0.77	ms	K0V	100.8010	0.248
EVRJ125134.08-790133.2	47428800	192.8920	−79.0259	10.32	9.09	0.57	ms	G8V	114.7710	0.157
EVRJ125505.76-851321.7	47199929	193.7740	−85.2227	11.73	6.37	0.38	ms	F3V	30.5570	0.083
EVRJ131324.31-792126.3	47375486	198.3513	−79.3573	12.28	6.37	0.31	ms	F7V	33.7030	0.228
EVRJ131504.46-763140.1	47445061	198.7686	−76.5278	12.08	7.84	0.69	ms	G9V	21.5120	0.055
EVRJ131906.34-840040.3	47206948	199.7764	−84.0112	11.58	5.87	1.07	giant	K3	23.8310	0.086
EVRJ131909.89-834711.0	47207423	199.7912	−83.7864	12.74	8.79	0.40	ms	F0V	15.7910	0.368
EVRJ132210.78-790543.1	47376460	200.5449	−79.0953	13.29	9.33	0.48	ms	F8V	37.6460	0.108
EVRJ132915.46-763040.0	47457701	202.3144	−76.5111	12.65	8.42	0.53	ms	F	19.3470	0.205
EVRJ133026.14-852532.2	47199044	202.6089	−85.4256	12.55	8.51	1.08	giant	K5	12.6020	0.038
EVRJ133347.26-833757.7	47210054	203.4469	−83.6327	13.39	8.35	0.56	ms	G3V	17.8470	0.057
EVRJ133848.86-834425.4	47209861	204.7036	−83.7404	13.58	10.16	0.58	ms	G7V	71.4170	0.455
EVRJ134321.74-845650.6	47199233	205.8406	−84.9474	12.78	8.18	0.55	ms	G5V	9.7290	0.365
EVRJ135211.09-844337.9	47201544	208.0462	−84.7272	13.73	9.53	0.60	ms	G8V	27.8460	0.382
EVRJ135212.36-785333.7	47399995	208.0515	−78.8927	12.07	6.17	0.59	ms	F9V	61.0300	0.443
EVRJ135431.18-815457.2	47214874	208.6299	−81.9159	11.19	6.69	0.26	ms	A4V	79.1580	0.050
EVRJ135907.01-842606.7	47203065	209.7792	−84.4352	13.05	7.80	0.42	ms	F7V	14.1710	0.324
EVRJ140102.93-823656.9	47212126	210.2622	−82.6158	10.79	9.06	0.75	ms	K0V	43.2894	0.188
EVRJ140546.42-835919.0	47203290	211.4434	−83.9886	11.29	8.38	0.76	ms	G9V	33.0580	0.044
EVRJ141018.94-830332.8	47211232	212.5789	−83.0591	11.89	4.11	0.21	ms	F1V	18.8112	0.123
EVRJ141043.54-834026.4	47204533	212.6814	−83.6740	12.19	10.85	0.86	ms	G3V	13.7081	0.045
EVRJ142633.19-825021.5	47205241	216.6383	−82.8393	12.92	11.70	0.75	ms	G9V	13.7050	0.176
EVRJ143328.56-833750.5	47202745	218.3690	−83.6307	12.77	8.89	0.68	ms	G5V	129.9480	0.420
EVRJ143842.46-813049.0	47228767	219.6769	−81.5136	13.07	8.39	0.67	ms	G1V	16.4483	0.153
EVRJ143916.73-844909.5	47178809	219.8197	−84.8193	12.18	6.11	0.55	ms	F	26.6630	0.082
EVRJ144001.37-842946.7	47201869	220.0057	−84.4963	12.67	7.87	0.42	ms	F6V	18.0120	0.126
EVRJ144437.08-775109.4	47397018	221.1545	−77.8526	12.23	4.31	0.30	ms	F1V	40.6480	0.151
EVRJ144607.85-835647.8	47202209	221.5327	−83.9466	12.20	8.33	0.73	ms	G6V	16.1201	0.081
EVRJ145302.21-823117.0	47219133	223.2592	−82.5214	12.80	8.93	0.87	ms	K0V	52.0750	0.236
EVRJ145519.22-761940.8	47504010	223.8301	−76.3280	13.50	5.89	0.71	ms	G7V	20.7599	0.242
EVRJ150051.41-823800.6	47219888	225.2142	−82.6335	11.69	7.50	1.42	giant	M2	50.1160	0.071
EVRJ150534.08-873605.8	47165613	226.3920	−87.6016	12.70	8.88	0.55	ms	F7V	178.9330	0.127
EVRJ151657.05-782900.6	47306697	229.2377	−78.4835	11.51	8.78	0.60	ms	G7V	155.4880	0.187
EVRJ152229.16-855039.1	47176529	230.6215	−85.8442	12.70	11.49	0.76	ms	K0V	55.5406	0.319
EVRJ152858.46-781119.0	47305454	232.2436	−78.1886	12.08	7.47	0.53	ms	F2V	37.9090	0.124
EVRJ152933.41-755721.2	47507129	232.3892	−75.9559	9.95	5.49	0.27	ms	A6V	27.9790	0.099
EVRJ153920.90-820531.2	47222149	234.8371	−82.0920	13.86	8.80	0.64	ms	G2V	21.6105	0.093
EVRJ154507.37-793351.1	47291578	236.2807	−79.5642	12.75	7.16	0.66	ms	G5V	12.6404	0.244

Table 11
(Continued)

ESID	APASSID	R.A. (J2000)	Decl. (J2000)	M_v	RPM	B-V	Size	Spec	Period (hours)	Depth (fractional)
EVRJ160954.46-851858.3	47181489	242.4769	−85.3162	12.76	7.60	0.33	ms	F4V	44.7430	0.189
EVRJ161508.66-835940.6	47187461	243.7861	−83.9946	13.18	11.16	0.73	ms	K0V	144.5400	0.403
EVRJ162303.89-810023.4	47253636	245.7662	−81.0065	12.34	3.25	0.56	ms	G7V	62.7963	0.313
EVRJ163423.28-841700.6	47182229	248.5970	−84.2835	13.63	9.48	0.99	ms	K2V	4.7610	0.397
EVRJ163736.60-853222.2	47181298	249.4025	−85.5395	12.70	6.11	0.67	ms	G2V	25.4995	0.076
EVRJ164003.19-835758.7	47185009	250.0133	−83.9663	12.91	9.45	0.57	ms	G6V	41.2660	0.247
EVRJ164326.83-861143.8	47180996	250.8618	−86.1955	14.13	7.55	0.86	ms	G	9.7203	0.336
EVRJ164433.50-860655.4	47181009	251.1396	−86.1154	12.22	5.87	0.59	ms	F1V	63.6382	0.219
EVRJ165236.34-775955.0	47279936	253.1514	−77.9986	12.57	6.78	0.53	ms	F9V	45.8782	0.215
EVRJ170835.06-804042.2	47250036	257.1461	−80.6784	13.36	10.77	0.64	ms	G6V	11.7251	0.185
EVRJ171020.11-794022.8	47266105	257.5838	−79.6730	13.38	9.62	0.60	ms	G0V	34.9601	0.224
EVRJ173306.41-841023.5	47184009	263.2767	−84.1732	11.94	7.48	0.01	ms	B8V	62.0777	0.107
EVRJ175021.89-833451.2	47241898	267.5912	−83.5809	12.90	10.55	0.45	ms	G1V	97.8154	0.670
EVRJ175151.98-770054.7	47705441	267.9666	−77.0152	12.99	7.95	0.60	ms	F1V	14.0583	0.312
EVRJ175821.86-823023.4	47246340	269.5911	−82.5065	13.32	8.36	0.68	ms	G6V	32.6439	0.272
EVRJ181441.14-755531.1	57414649	273.6714	−75.9253	11.71	9.14	0.66	ms	G3V	70.3589	0.235
EVRJ181713.66-870538.4	57073210	274.3069	−87.0940	11.79	12.45	0.66	ms	K0V	8.4675	0.138
EVRJ181714.18-773047.2	57406134	274.3091	−77.5131	13.02	7.02	0.51	ms	G1V	36.9321	0.603
EVRJ181841.30-822733.5	57161826	274.6721	−82.4593	12.83	3.05	0.62	giant	G2	76.6038	0.070
EVRJ184428.49-823046.8	57160536	281.1187	−82.5130	13.66	9.22	0.54	ms	G8V	71.0168	0.238
EVRJ184600.48-775012.5	57197233	281.5020	−77.8368	12.93	8.55	0.56	ms	G1V	37.1489	0.192
EVRJ185649.78-802355.0	57169339	284.2074	−80.3986	12.77	8.40	0.71	ms	K1V	11.4201	0.128
EVRJ190936.96-825733.8	57102741	287.4040	−82.9594	12.21	9.17	0.81	ms	K1V	20.9770	0.097
EVRJ191030.65-852500.5	57093523	287.6277	−85.4168	13.72	7.03	0.40	ms	F8V	69.7130	0.580
EVRJ191957.17-815827.8	57163432	289.9882	−81.9744	11.82	8.40	0.76	ms	G9V	49.7553	0.190
EVRJ195938.52-800854.6	57171413	299.9105	−80.1485	13.38	8.73	0.66	ms	G6V	11.8792	0.362
EVRJ200844.69-841100.6	57097190	302.1862	−84.1835	12.36	6.21	0.74	ms	G8V	25.0280	0.183
EVRJ204029.23-792542.2	57173726	310.1218	−79.4284	12.04	7.83	0.74	ms	G8V	27.8260	0.149
EVRJ211629.93-755719.1	57218408	319.1247	−75.9553	11.50	8.69	0.41	ms	F4V	15.3512	0.213
EVRJ213512.74-762221.4	57148511	323.8031	−76.3726	13.06	9.38	0.70	ms	G4V	21.3854	0.100
EVRJ214611.09-783816.4	57142128	326.5462	−78.6379	13.01	7.87	0.74	ms	K1V	58.0007	0.138
EVRJ215221.58-830052.9	57089418	328.0899	−83.0147	12.85	3.57	1.43	giant	M2	14.9228	0.069
EVRJ215337.54-775041.6	57143831	328.4064	−77.8449	12.46	10.23	0.66	ms	G4V	4.7476	0.086
EVRJ215538.66-830823.6	57089350	328.9111	−83.1399	12.97	9.49	0.77	ms	G9V	14.9228	0.095
EVRJ223125.73-803027.7	57127400	337.8572	−80.5077	11.82	5.48	0.58	ms	F9V	41.7888	0.068
EVRJ223812.41-780109.1	57136882	339.5517	−78.0192	13.50	10.29	0.38	ms	A8V	15.0893	0.256
EVRJ225743.22-782429.2	57136245	344.4301	−78.4081	11.86	8.36	0.49	ms	G6V	19.8070	0.071
EVRJ225936.22-830757.0	57083769	344.9009	−83.1325	11.22	9.34	0.69	ms	K0V	12.8218	0.064
EVRJ230355.18-773000.7	57137831	345.9799	−77.5002	12.58	8.47	0.59	ms	G2V	34.7999	0.138
EVRJ231712.07-790607.6	57132830	349.3003	−79.1021	11.51	8.15	0.66	ms	G6V	195.0140	0.154
EVRJ232322.32-771336.5	57135188	350.8430	−77.2268	12.43	5.89	0.71	ms	G6V	66.0742	0.196
EVRJ233038.69-760536.6	57261482	352.6612	−76.0935	12.56	9.29	0.60	ms	G0V	84.7218	0.390
EVRJ234021.77-780703.4	57134048	355.0907	−78.1176	13.66	8.99	0.47	ms	F8V	11.6461	0.136
EVRJ234130.91-790731.8	57133414	355.3788	−79.1255	13.36	7.75	0.53	ms	F5V	90.6906	0.291

Note. Columns 1–5 are identification numbers, right ascension, declination, and magnitude. Columns 6–9 are the reduced proper motion (RPM), and color difference (B-V), which we use to estimate the star size and spectral type (see Section 4.2.1). Columns 10 and 11 are the period found in hours, and the fractional eclipse depth from normalized flux.

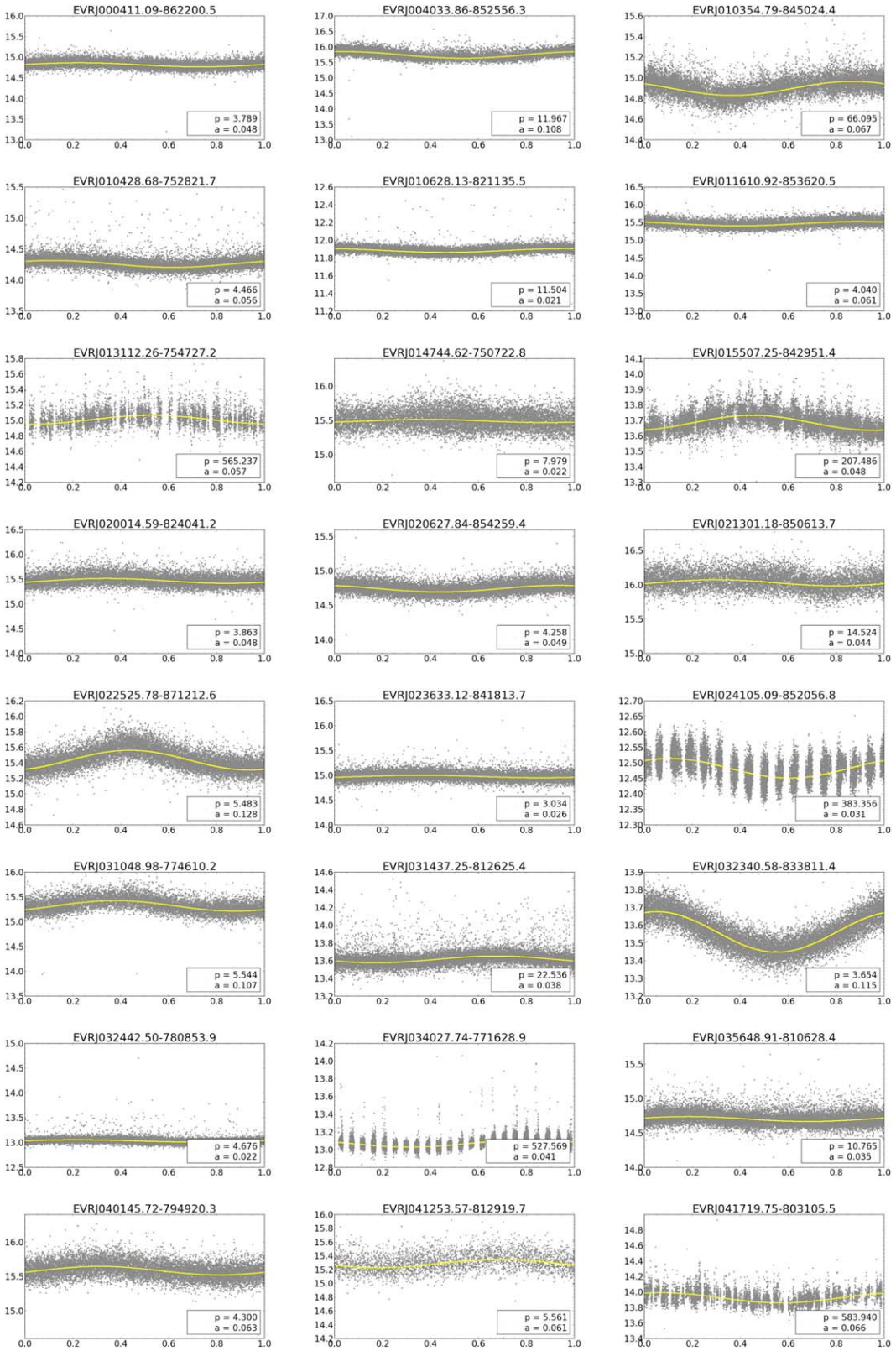

Figure 16. Variable star discoveries. *Y*-axis is instrument magnitude, *x*-axis is the phase, p = period found in hours, a = amplitude change in magnitude. Gray points are two minute cadence, yellow is the best LS fit.

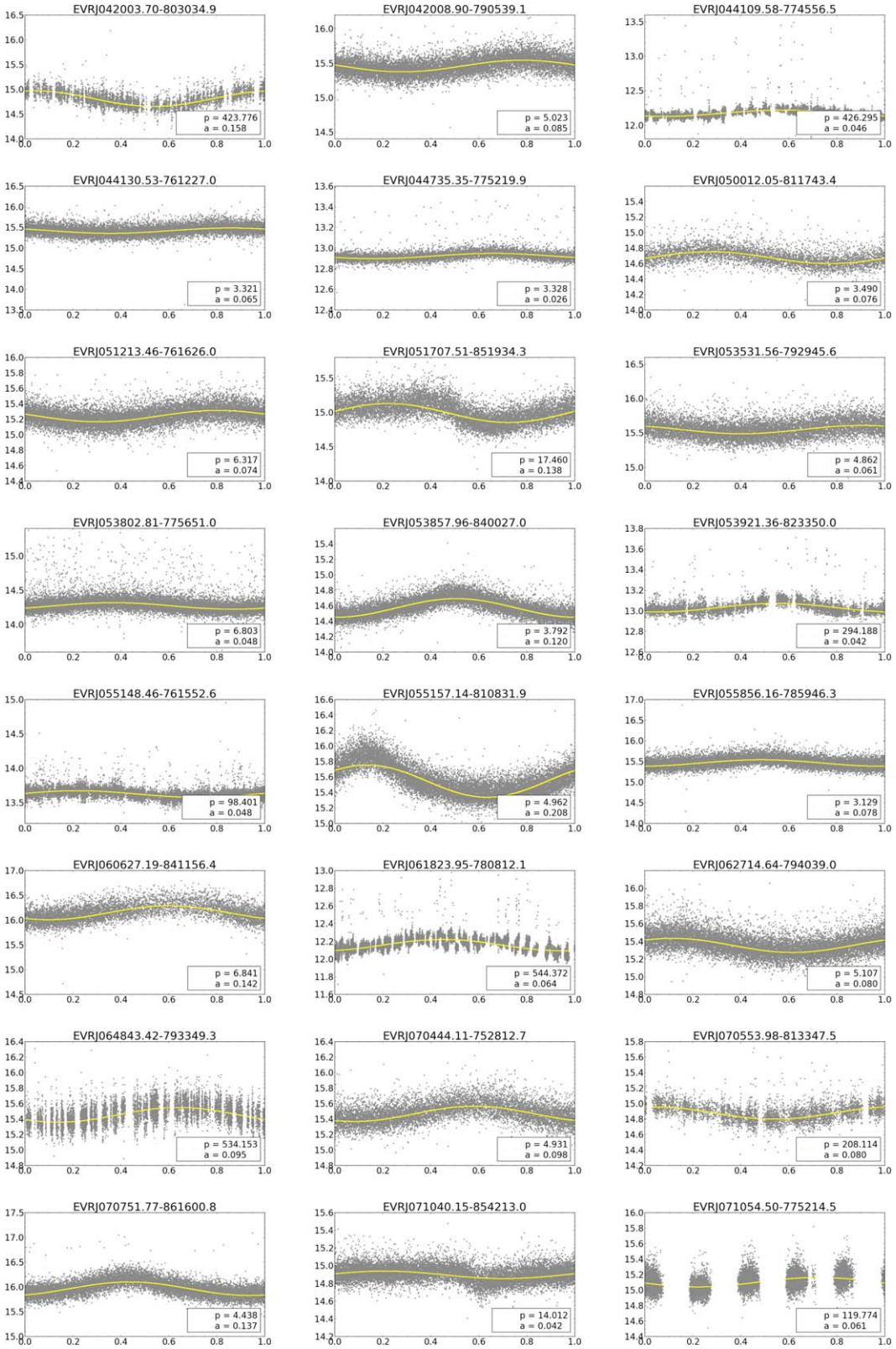

Figure 16. (Continued.)

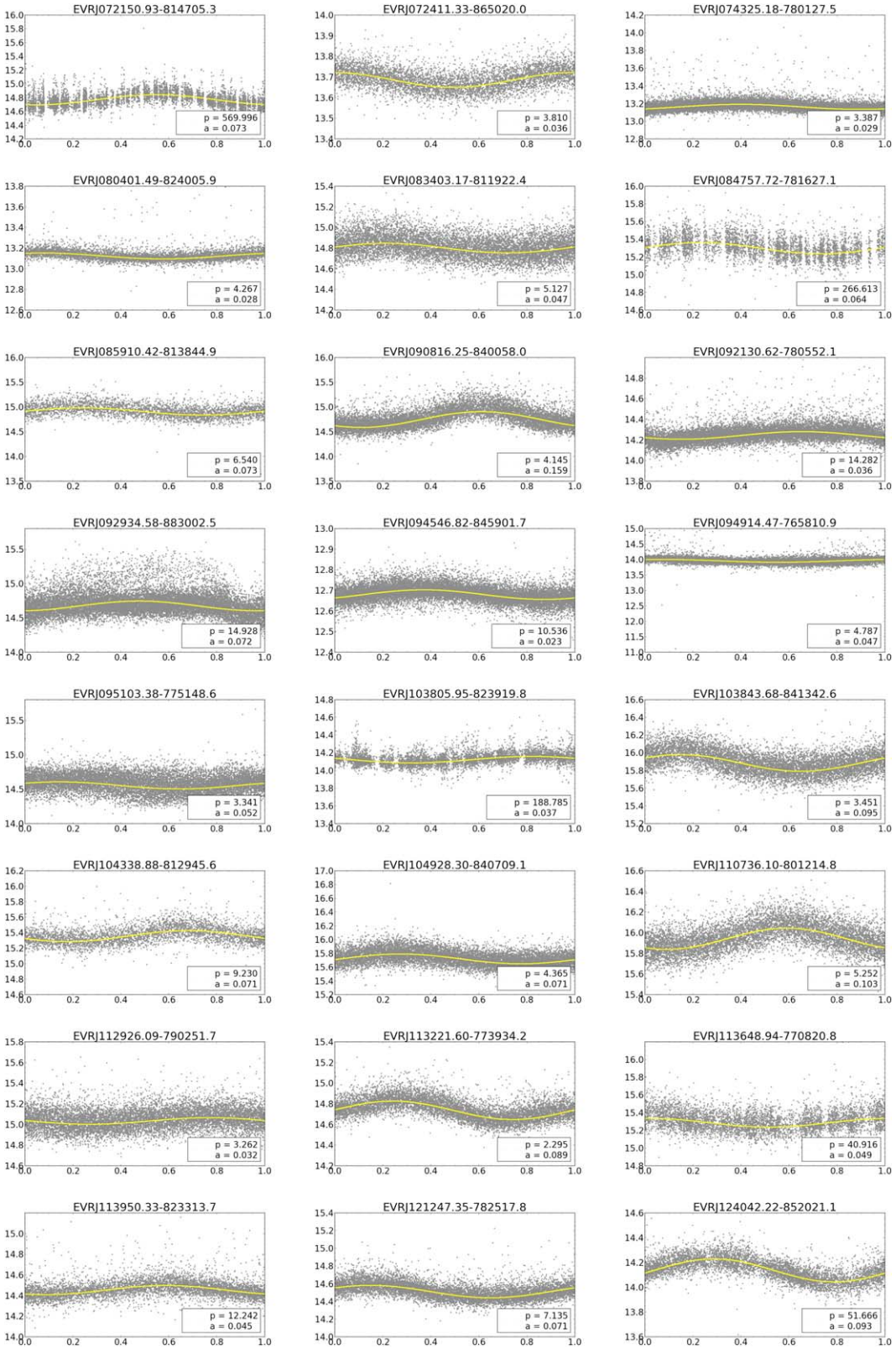

Figure 16. (Continued.)

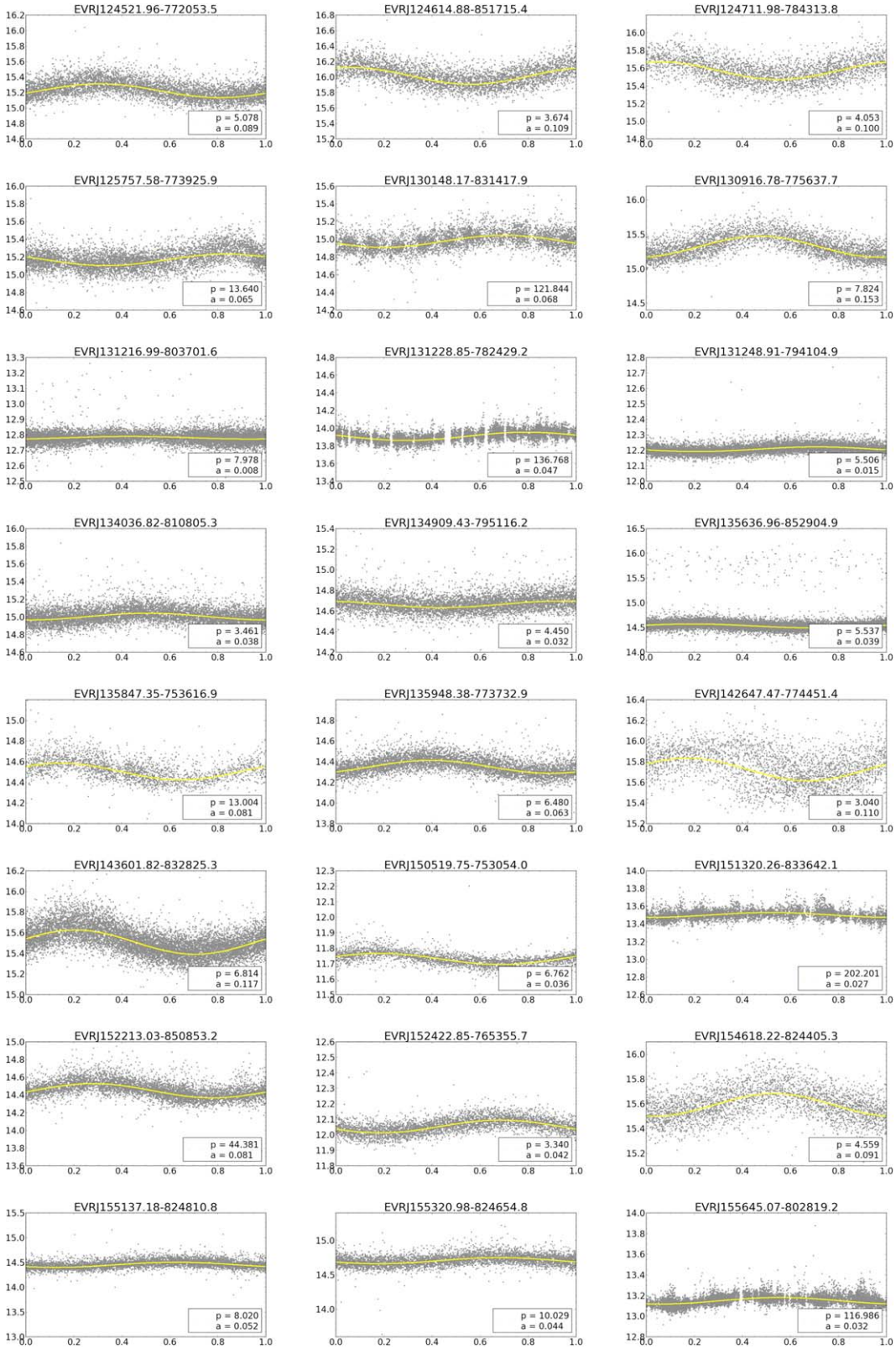

Figure 16. (Continued.)

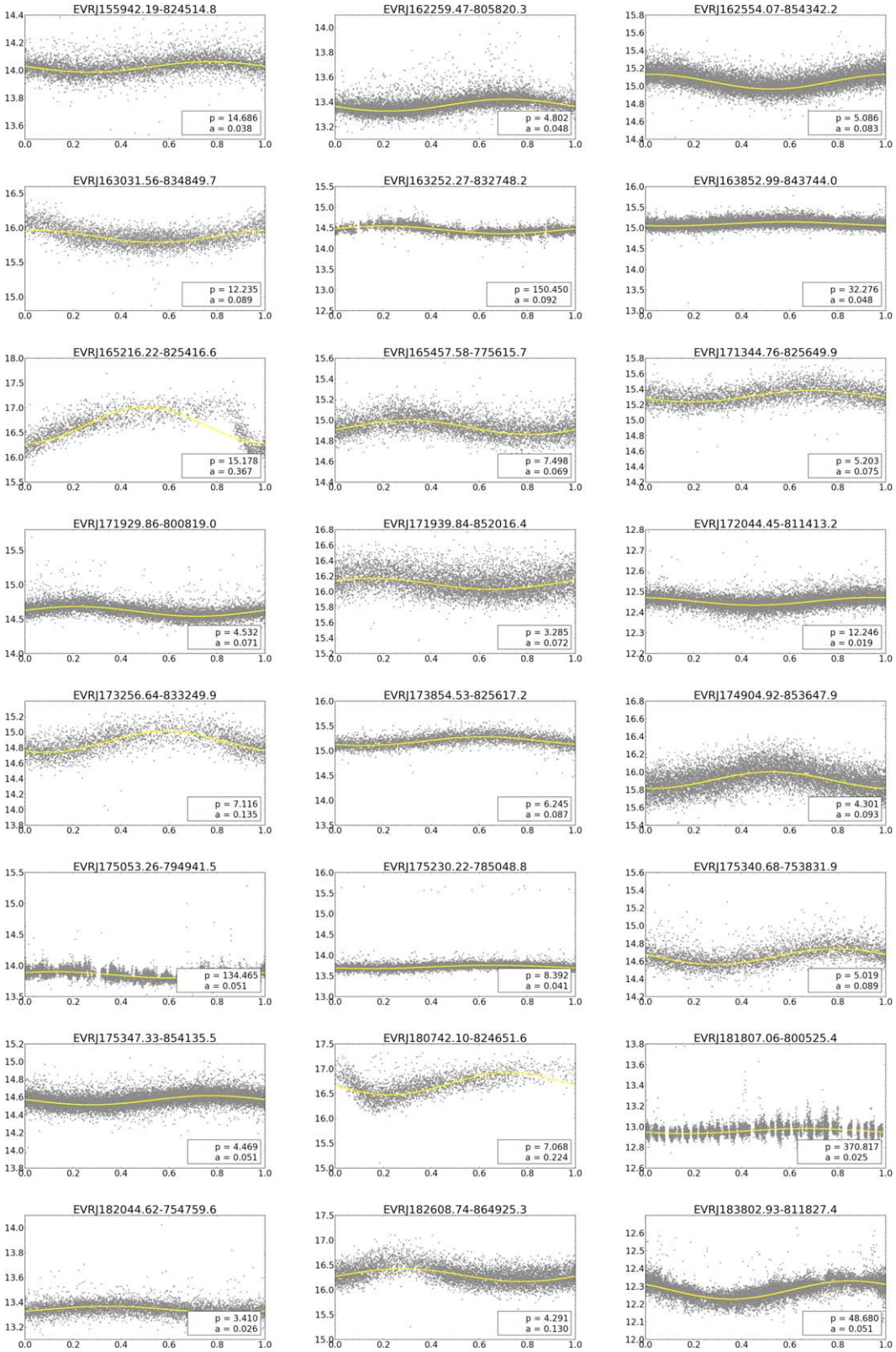

Figure 16. (Continued.)

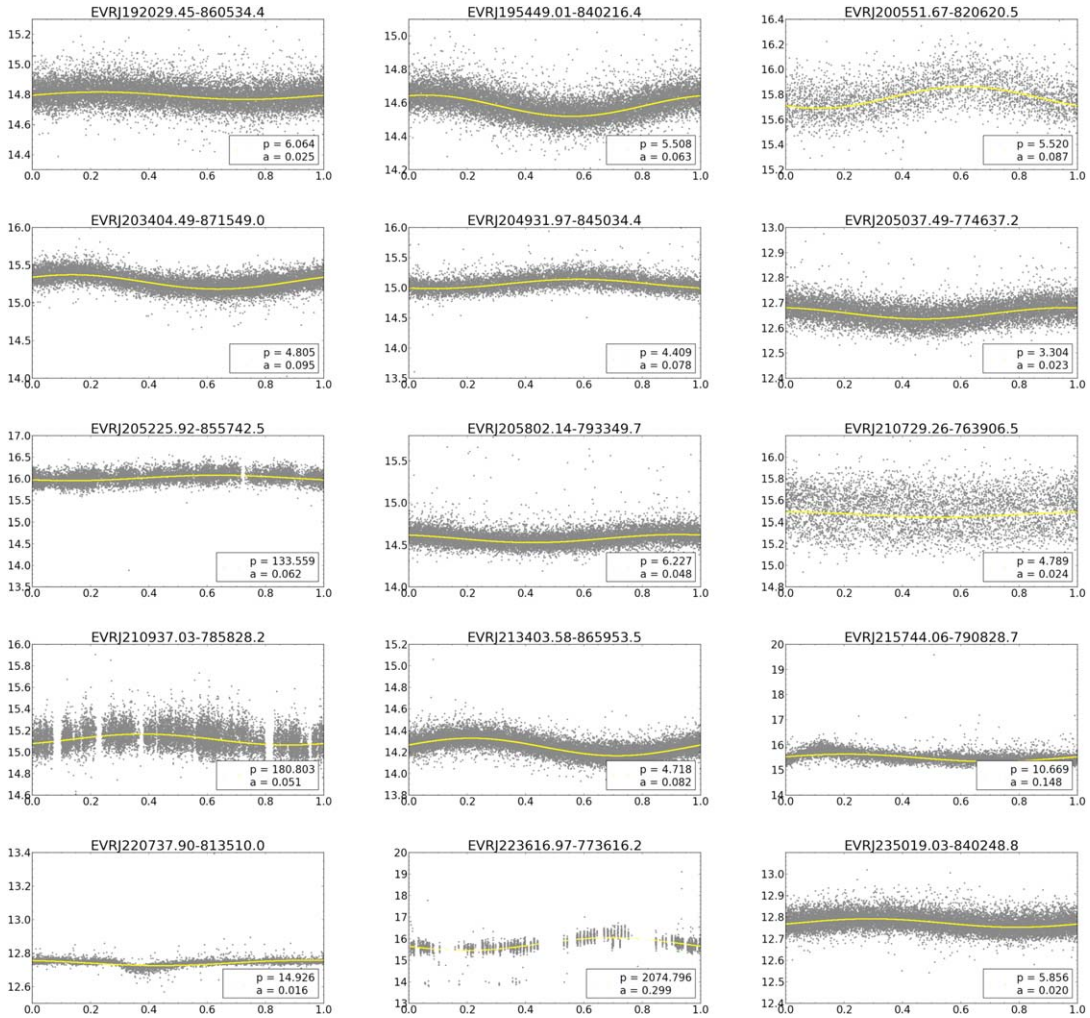

Figure 16. (Continued.)

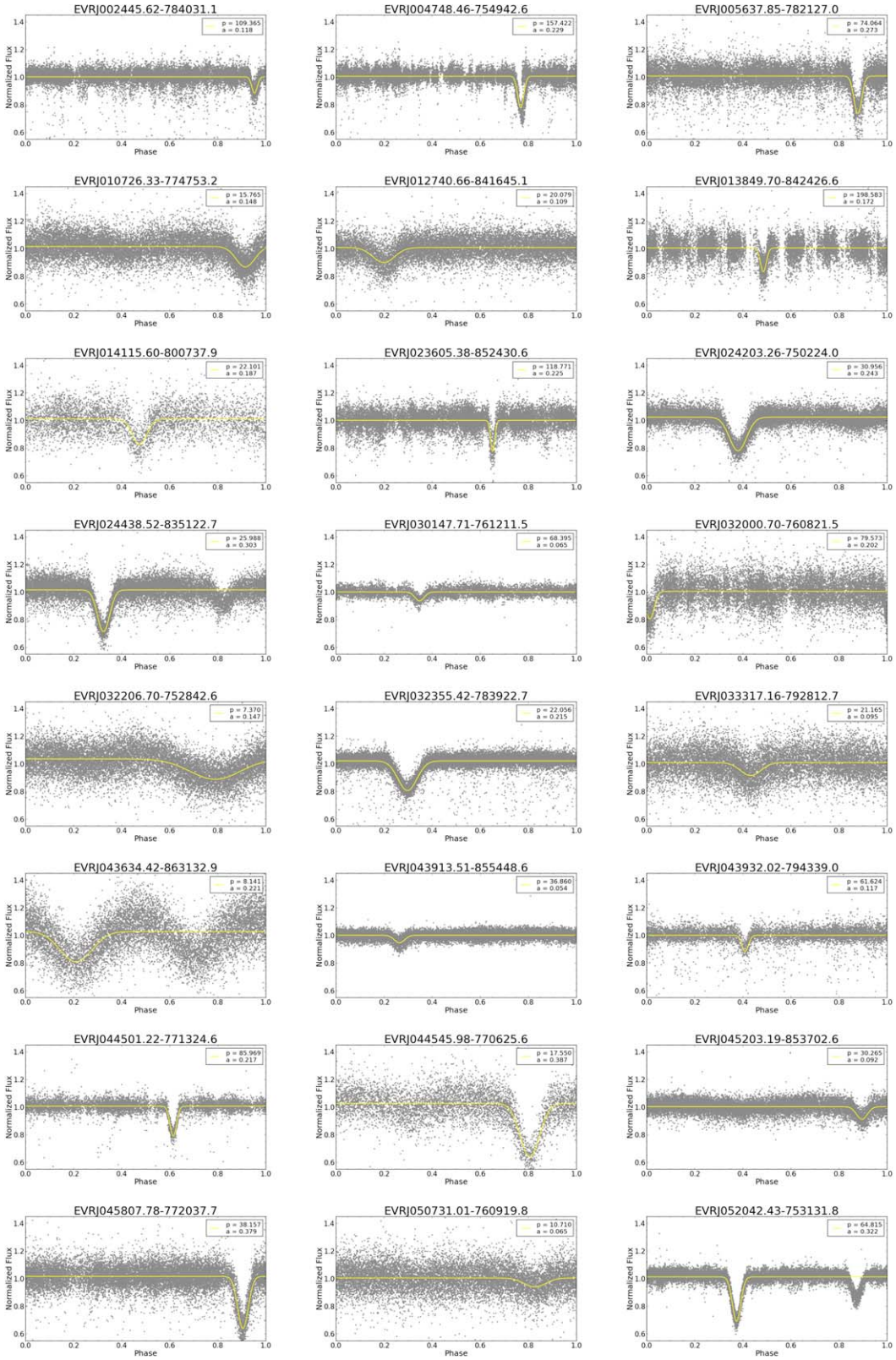

Figure 17. Eclipsing Binary discoveries. *Y*-axis is normalized flux, *x*-axis is the phase, p = period found in hours, a = eclipse depth. Gray points are two minute cadence, yellow is the best fit.

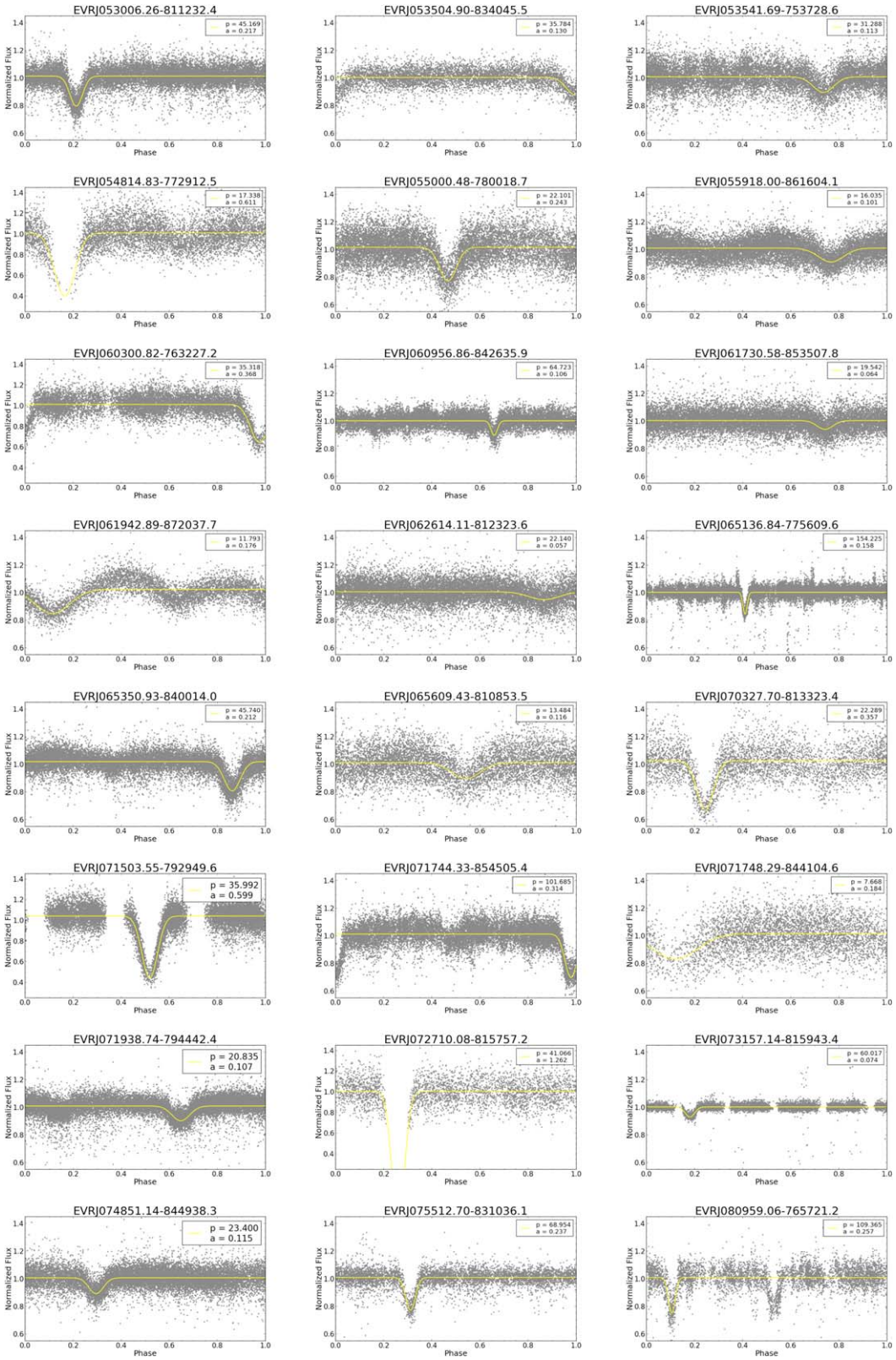

Figure 17. (Continued.)

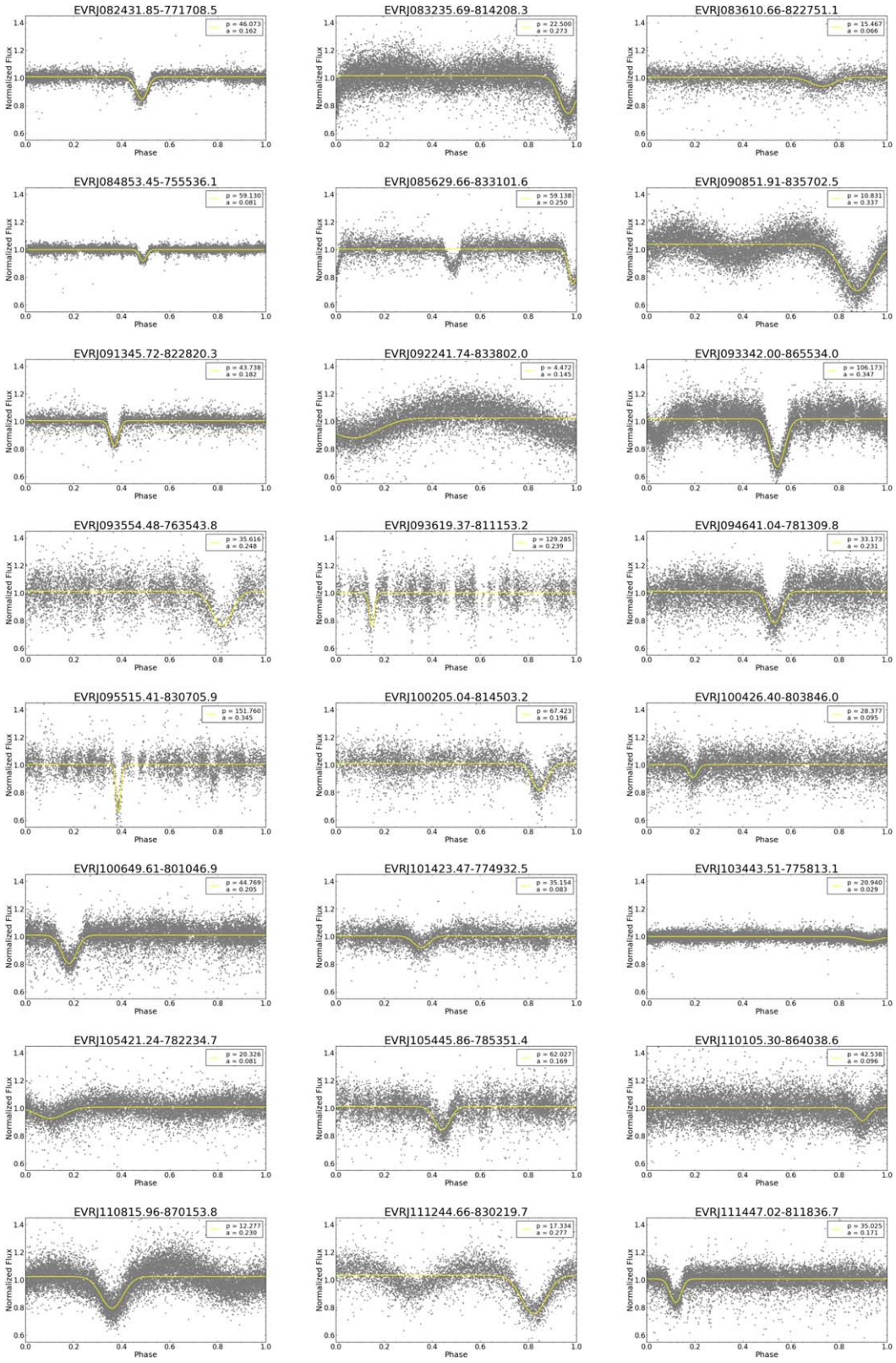

Figure 17. (Continued.)

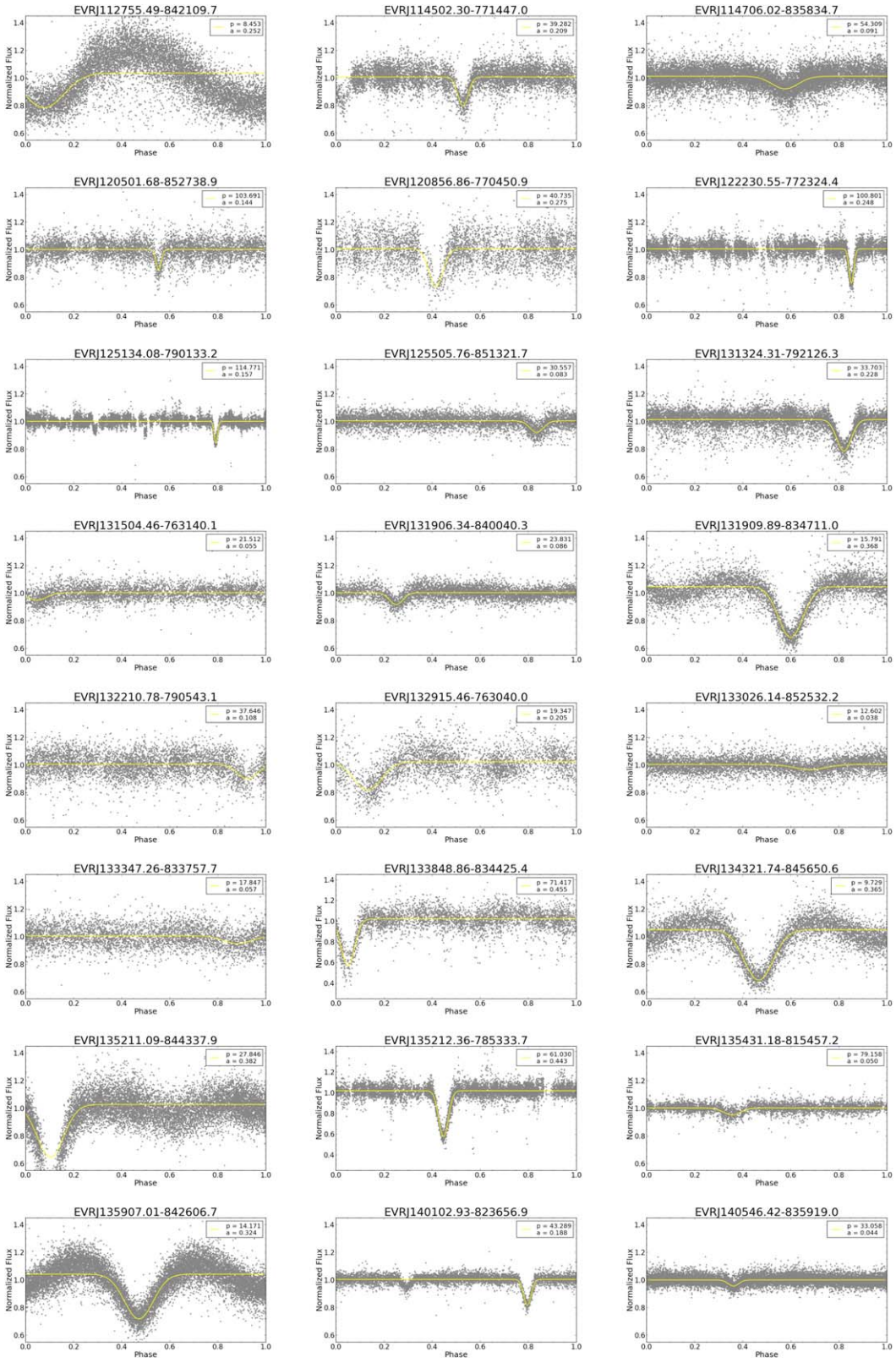

Figure 17. (Continued.)

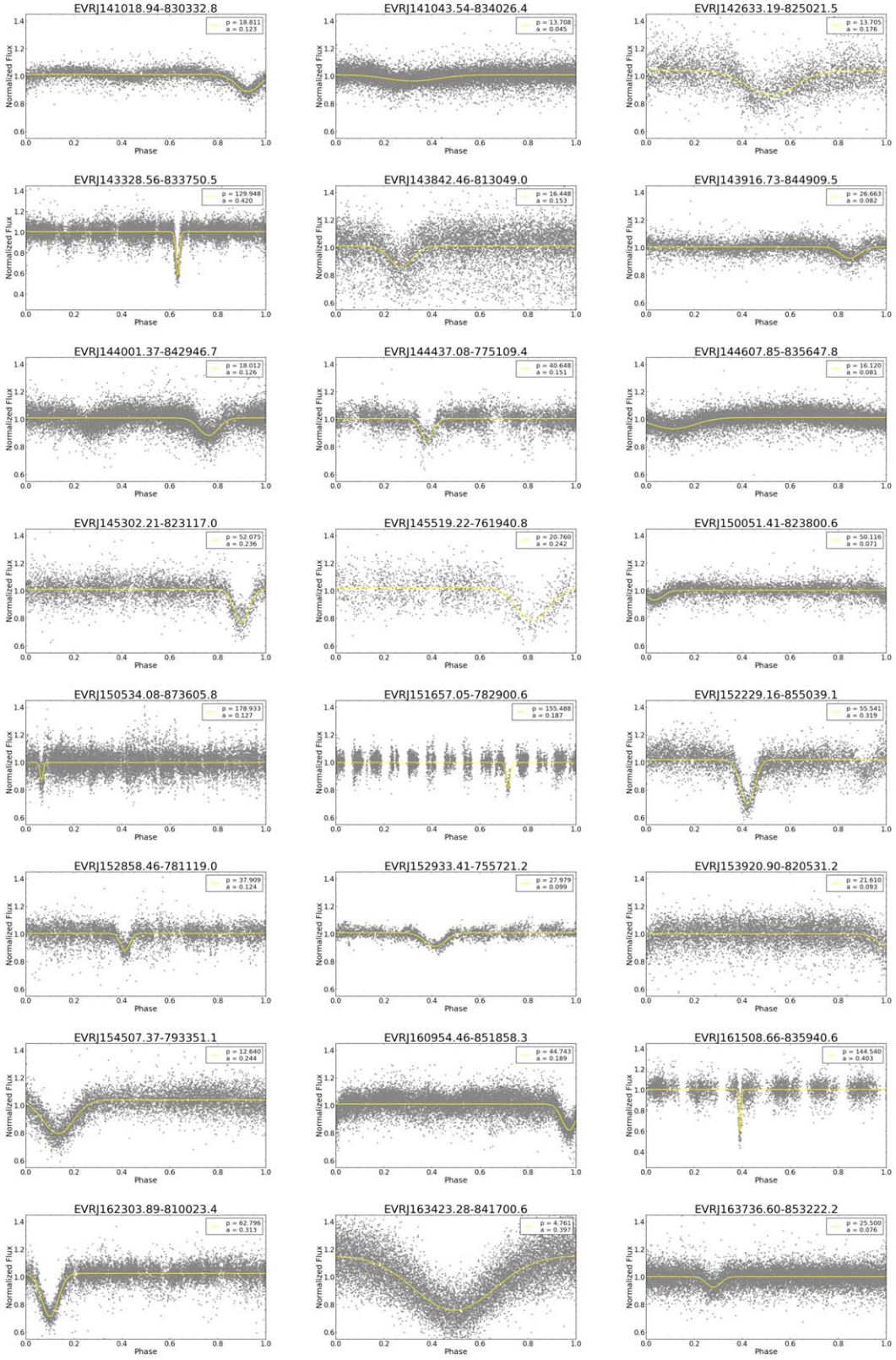

Figure 17. (Continued.)

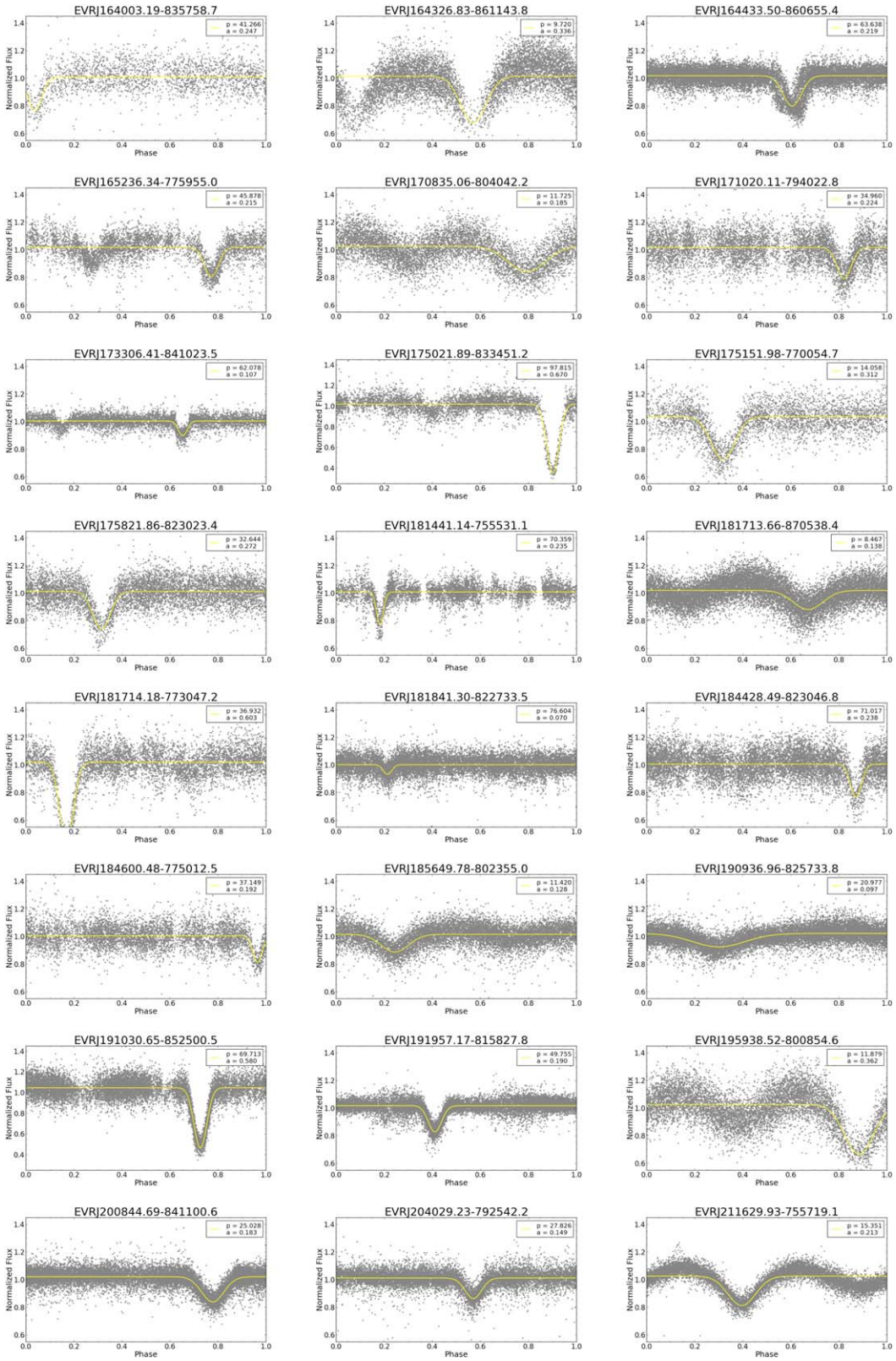

Figure 17. (Continued.)

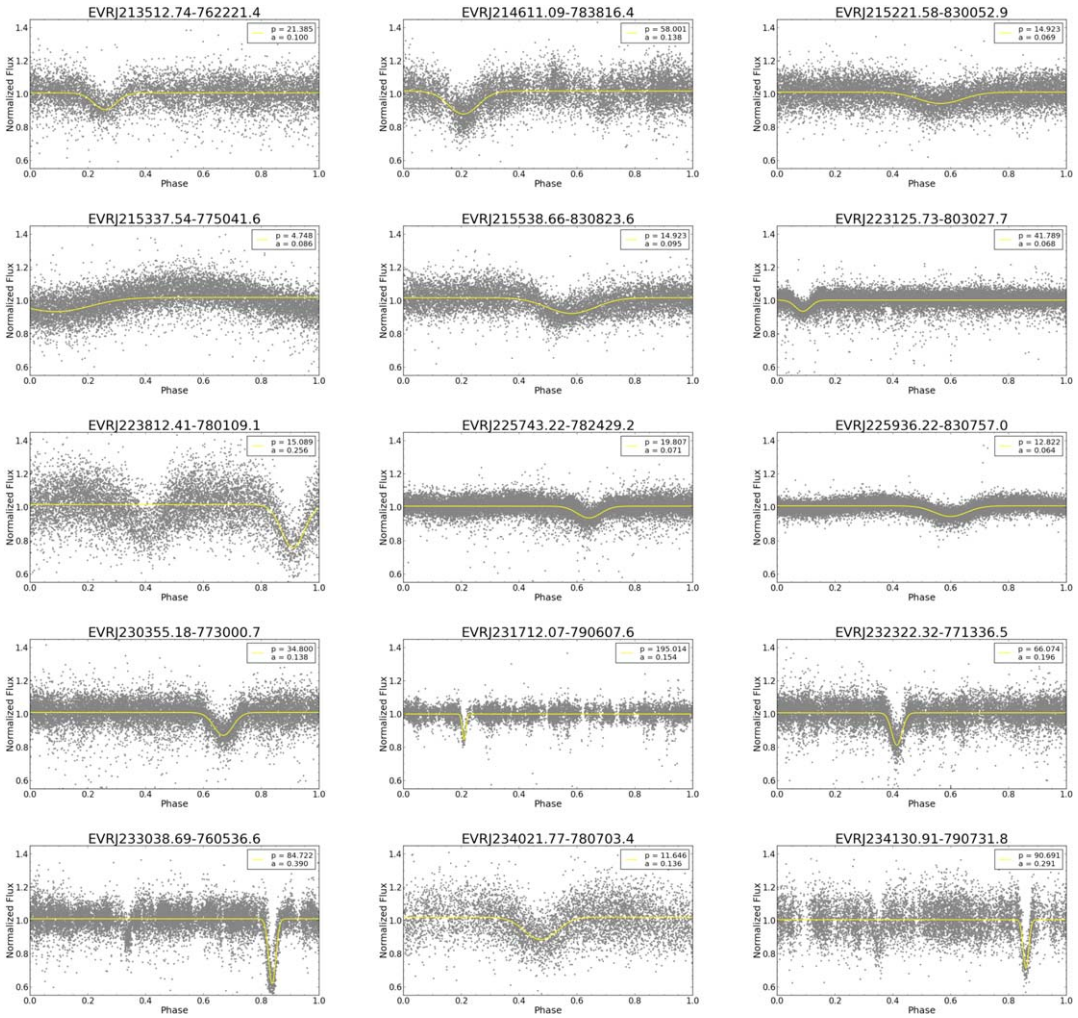

Figure 17. (Continued.)

References

Bakos, G., Noyes, R. W., Kovács, G., et al. 2004, PASP, 116, 266
Bakos, G. Á. 2018, in Handbook of Exoplanets, ed. H. Deeg & J. Belmonte (Cham: Springer), 957
Chaturvedi, P., Sharma, R., Chakraborty, A., Anandarao, B. G., & Prasad, N. J. S. S. V. 2018, AJ, 156, 27
Christ, C. N., Montet, B. T., & Fabrycky, D. C. 2019, AJ, 157, 235
Clemens, J. C., Crain, J. A., & Anderson, R. 2004, Proc. SPIE, 5492, 331
Collins, K. A., Kielkopf, J. F., Stassun, K. G., & Hessman, F. V. 2017, AJ, 153, 77
Covey, K. R., Ivezić, Ž., Schlegel, D., et al. 2007, AJ, 134, 2398
Fuchs, J. T., Dunlap, B. H., Clemens, J. C., et al. 2017, in ASP Conf. Ser. 509, 20th European White Dwarf Workshop ed. P. E. Tremblay, B. Gaensicke, & T. Marsh (San Francisco, CA: ASP), 263
Gaia Collaboration, Brown, A. G. A., Vallenari, A., et al. 2018, A&A, 616, A1
Geier, S., Østensen, R. H., Nemeth, P., et al. 2017, OAst, 26, 164
Henden, A. A., Levine, S., Terrell, D., & Welch, D. L. 2015, AAS Meeting, 225, 336.16
Jones, E. 1972, ApJ, 173, 671
Kharchenko, N. V. 2001, KFNT, 17, 409
Kovacs, G., Zucker, S., & Mazeh, T. 2002, A&A, 391, 369
Kraus, A. L., Ireland, M. J., Martinache, F., & Hillenbrand, L. A. 2011, ApJ, 731, 8
Kraus, A. L., Douglas, S. T., Mann, A. W., et al. 2017, ApJ, 845, 72
Law, N. M., Kulkarni, S. R., Dekany, R. G., et al. 2009, PASP, 121, 1395
Law, N. M., Kraus, A. L., Street, R., et al. 2012, ApJ, 757, 133
Law, N. M., Carlberg, R., Salbi, P., et al. 2013, AJ, 145, 58
Law, N. M., Fors, O., Ratzloff, J., et al. 2015, PASP, 127, 234
Lépine, S., & Gaidos, E. 2011, AJ, 142, 138
Lomb, N. R. 1975, Ap&SS, 39, 447
Mann, A. W., Feiden, G. A., Gaidos, E., Boyajian, T., & von Braun, K. 2015, ApJ, 804, 64
Mayor, M., Pepe, F., Queloz, D., et al. 2003, Msngr, 114, 20
Merline, W. J., & Howell, S. B. 1995, ExA, 6, 163
Ofir, A. 2014, A&A, 561, A138
Pecaut, M. J., & Mamajek, E. E. 2013, ApJS, 208, 9
Pedregosa, F., Varoquaux, G., Gramfort, A., et al. 2011, Journal of Machine Learning Research, 12, 2825 (http://www.jmlr.org/papers/v12/pedregosa11a.html)
Pepper, J., Pogge, R. W., DePoy, D. L., et al. 2007, PASP, 119, 923
Pietro Gentile Fusillo, N., Gaensicke, B. T., & Greiss, S. 2015, arXiv:1501.05309

Pietro Gentile Fusillo, N., Raddi, R., Gänsicke, B. T., et al. 2017, arXiv:1703.09714
Pollacco, D. L., Skillen, I., Collier Cameron, A., et al. 2006, PASP, 118, 1407
Press, W. H., Teukolsky, S. A., Vetterling, W. T., & Flannery, B. P. 2007, Numerical Recipes 3rd Edition: The Art of Scientific Computing (3rd ed.; New York: Cambridge Univ. Press)
Raddi, R., Gentile Fusillo, N. P., Pala, A. F., et al. 2017, MNRAS, 472, 4173
Ratzloff, J. K., Law, N. M., Fors, O., et al. 2019, PASP, 131, 075001
Reichart, D., Nysewander, M., Moran, J., et al. 2005, NimC, 28, 767
Ricker, G. R., Winn, J. N., Vanderspek, R., et al. 2014, Proc. SPIE, 9143, 914320
Roeser, S., Demleitner, M., & Schilbach, E. 2010, AJ, 139, 2440
Scargle, J. D. 1982, ApJ, 263, 835
Stassun, K. G., Oelkers, R. J., Pepper, J., et al. 2018, AJ, 156, 102
Tamuz, O., Mazeh, T., & Zucker, S. 2005, MNRAS, 356, 1466
Tokovinin, A., Fischer, D. A., Bonati, M., et al. 2013, PASP, 125, 1336
Tonry, J. L. 2011, PASP, 123, 58
Torres, G. 2010, AJ, 140, 1158
Wang, S., Zhang, H., Zhou, X., et al. 2015, ApJS, 218, 20
Wenger, M., Ochsenbein, F., Egret, D., et al. 2000, A&AS, 143, 9
Young, A. T. 1967, AJ, 72, 747